ELECTRO-THERMAL SIMULATION STUDIES OF

SINGLE-EVENT BURNOUT IN POWER DIODES

By

Sameer V. Mahajan

Thesis

Submitted to the Faculty of the

Graduate School of Vanderbilt University

in partial fulfillment of the requirements

for the degree of

MASTER OF SCIENCE

in

Interdisciplinary Materials Science

August, 2006

Nashville, Tennessee

Approved:

Professor D. Greg Walker

Professor Ronald D. Schrimpf

ACKNOWLEDGEMENTS

TABLE OF CONTENTS

LIST OF TABLES

LIST OF FIGURES

CHAPTER I

INTRODUCTION

Electronic systems positioned in space are exposed to various forms of radiation. The space radiation environment consists of solar rays, cosmic rays and protons and electrons trapped in radiation belts [1, 2]. Interaction of electronic systems with ionizing radiation could affect their performance, leading to premature failure. Reliability of these electronic systems is very important because of the high costs of space systems. A complete understanding of fundamental mechanisms of failure in electronic systems is necessary to improve their reliability.

A single-event effect (SEE) can be defined as the temporary or permanent failure of an electronic device due to interaction with an energetic particle. Single-event effects have been observed in a variety of space as well as terrestrial electronic systems [3, 4]. Solar rays and heavy ions are mainly responsible for the failures in space systems, while neutrons, protons, and pions cause failures in terrestrial systems. Single-event burnout (SEB) is a type of single-event effect, which is characterized by a permanent failure caused by physical damage.

Power devices (high current, high voltage devices) are widely used in space-based electronic systems. The very large electric fields present in power devices could prove lethal when an ionizing particle creates a dense filament of electron-hole pairs.

Burnout mechanism in power MOSFETs

SEB in power metal-oxide-semiconductor field-effect transistor (MOSFET) system was noticed by Waskiewicz et al [5]. Considerable effort has been devoted to understanding breakdown mechanisms in n-channel MOSFETs with experimental [6-8] and simulation techniques [9]. The parasitic *npn* bipolar structure inherent to n-channel MOSFETs was identified to play a key role in the burnout mechanism. The drain-substrate junction is reverse-biased in n-channel MOSFETs. When an energetic particle passes through the junction, the generated electron-hole pairs separate under the influence of the electric field, producing current. The current across the reverse-biased junction may turn on the parasitic *npn* transistor. The resulting large currents and high voltages may generate high power, leading to burnout of the MOSFET.

Burnout of power diodes

Catastrophic failures in power diodes were first observed by Kabza when DC stress tests were performed on power diodes operating at rated conditions [10]. When the same tests were performed 140 m below ground, failure rates dropped significantly. Cosmic radiation was identified as a cause of failures. The failure rate was exponentially dependent on applied bias. Simulation studies predicted high avalanche-generated charge compared to deposited charge for high voltages. Thus high local power densities causing localized self-heating leading to burnout were thought to be responsible for failures. Current transients were simulated for different numbers of strike-induced carriers. Simulations indicated that peak temperature inside the device exceeds the silicon melting temperature above a total number of 5×10^{10} strike-induced electron-hole pairs within the

track creating high carrier density. A particle possessing 180 GeV is required to generate this number of carriers. However, particle rates for these energies are lower than observed failure rates. Thus it was found that solely radiation-induced charges do not predict device failure due to self-heating. Zeller developed a phenomenological model describing the failure rate based on its exponential dependence on applied bias [11]. This model produced a good fit with the experimental data, indicating its applicability for device design. The burnout mechanism was still unidentified. The thermal runaway phenomenon was reported in 2-D simulation studies of non-planar GTO-Thyristors while studying the effects of different cooling conditions [12]. A thermodynamic model of thermoelectric transport predicted accelerated thermal runaway process.

Voss et al. performed irradiation experiments with C^{12} ions possessing different energies [13]. Irradiation was started at 2000 V of blocking voltage, and applied bias was increased 100 V per minute of exposure. All the devices failed due to irradiation. Charge collection spectra taken during the study indicated noticeable charge multiplication above 2400 V. The failures were attributed to triggering of nuclear reactions in the device, not necessarily near the *pn* junction.

Busatto et al. studied single-event burnout in power diodes using bombardment of Si^{28} ions possessing energies of 108 MeV and 156 MeV [14]. Charge collection and current traces for the diode were recorded. Deposited charge was independent of applied bias, but secondary charge generation was found to be dependent on the applied bias. Also, a secondary increase in collected charge was different for ions possessing different

3

energies. Initiation of secondary charge collection was found to be dependent on the energy of the ion. Figure 1 shows fraction of secondary charge generation as a function of applied bias for two different ion energies (108 MeV and 156 MeV). It was found that higher applied voltage is necessary to generate same secondary charge fraction for more energetic ions. For example, 70% of the total secondary charge is estimated to be generated at the applied bias of 780 V for 108 MeV ions, while for 156 MeV ions the diode needs to be biased at 955 V (refer Figure 1).
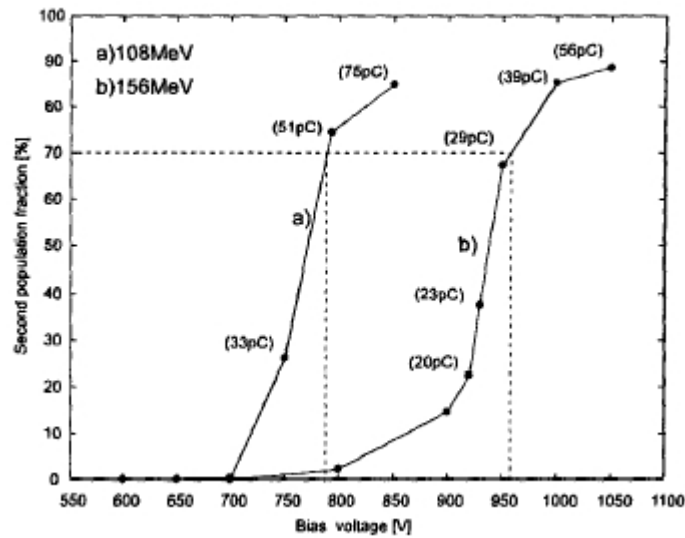
Figure 1 Secondary charge generation fraction vs. applied bias for different ion-energies [14].

Another study was performed by Soelkar et al. with bombardment of high energy carbon and Krypton ions; current waveforms and charge spectra were recorded [15]. The generated charge was found to be dependent on bias. The current trace for proton-irradiated samples indicated secondary current that was associated with thermal breakdown [15]. However, the thermal breakdown mechanism was not confirmed with

4

further analysis. 2-D axi-symmetric electrical simulations were performed to observe the internal electric field evolution after the strike. Figure 2 shows spatial and temporal profile of electric field along diode depth in the ion incident plane. The range of C^{12} ion (17 MeV) is short (16 μm) compared to diode depth (450 μm). Deposited charge density increases along the ion track, which peaks at the end of the track. The charges deposited during the strike modify the potential distribution. This results in localized electric field variation. The electric field peak occurs at the end of the ion track. The charges move towards the contacts because of drift and in radial direction due to the diffusion. Thus the electric field peak moves to the cathode as the carrier distribution changes along the ion path. The peak electric field diminishes in time as carriers are swept out of the diode and carrier distribution moves towards steady state equilibrium.
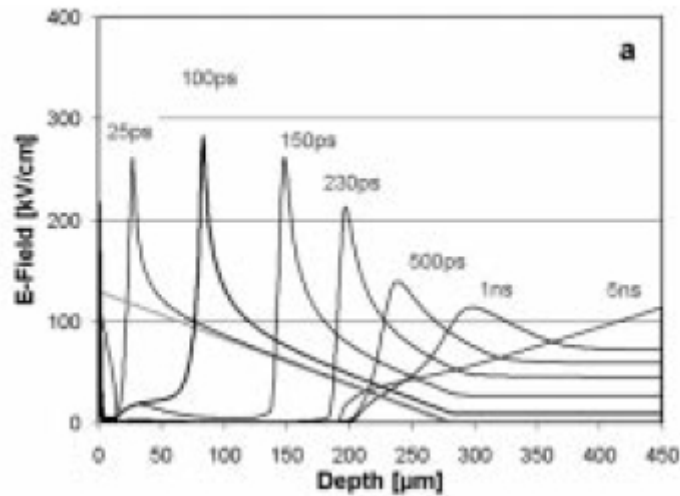
Figure 2 Simulation of the spatial and temporal evolution of the internal electric field in a 4 kV diode for C^{12} (17 MeV) ion. Applied bias = 1800 V [15].

Ironically, diodes are generally much simpler devices than MOSFETs, yet understanding of SEB in these elementary devices is limited. The inherent bipolar structures responsible

for failure in power MOSFETs do not exist in diodes [16]. There is no corresponding electrical feedback mechanism to maintain a strike-induced current until the device destroys itself.

The experimental and simulation studies performed so far have failed to identify the burnout breakdown mechanism for power diodes. Although the possibility of thermal breakdown has been suggested with preliminary results, enough attention has not been given to the thermal effects. Recently, Al-Badri *et al* observed single event burnout of power diode using coupled electro-thermal simulations [17]. The effect of irradiation of 17-MeV C^{12} ions was simulated. When diode was biased at 2700 V and above, large increase in the current along with temperature rise reaching melting point of silicon was observed indicating diode burnout. The breakdown is attributed to the local heat generation due to impact ionization-generated charge. Presence of thermal feedback loop is hypothesized earlier [18]. Local temperatures inside diode increase due to presence of high current and electric field following ion strike. Intrinsic carrier concentration, which is also a function of temperature, increases with temperature. As the intrinsic carrier concentration increases at high temperatures, more carriers are available, producing large current. A thermal feedback loop may be initiated where an increase in current leads to more heating.

Scope and organization of the thesis

The goal of the present work is to identify the burnout mechanism in power diodes using electrical-thermal simulations. A simplified 2-D power diode structure is modeled for

which single-event burnout was observed experimentally. Coupled electro-thermal simulations that include thermal effects are performed. Temperature-dependent mobility, recombination and intrinsic carrier concentration are employed. The simulation technique enables isolation of impact ionization to identify its contribution in strike-induced current. Also, the effect of applied bias on strike-induced current is studied at three different applied biases. Isothermal ion-strike simulations at different temperature are performed to understand the effect of temperature on the ion-induced current transient. Non-isothermal ion-strike simulations on the power diode at different applied biases are performed. Peak temperature inside the power diode is monitored in time. The results are compared with the published data and analyzed to explain the breakdown of the diode.

Chapter I of the thesis introduces the single-event burnout phenomenon observed in power devices such as power MOSFETS and power diodes. Experimental and simulation studies performed by the scientific community to identify failure mechanisms are summarized. Chapter II covers the fundamental physics describing *pn*-junction diodes. The steady-state electrical characteristics of diode are described with the help of supporting device-physics concepts. In Chapter III, various non-equilibrium phenomena that may occur during semiconductor device operation are discussed. The carrier and energy transport mechanisms that explain motion of the carriers under non-equilibrium conditions are reviewed. Chapter IV includes the simulation methodology followed for modeling the power diode. Various isothermal and non-isothermal simulations performed in a logical pattern to study the single-event burnout mechanism are listed; the results are

discussed and compared with reported data wherever possible. The results of the simulation studies are summarized in Chapter V.

CHAPTER II

DIODE THEORY

A *pn* junction is a component of most microelectronic devices. A diode is the simplest device, having a single *pn* junction, while many other devices have multiple *pn* junctions. In the present work, single-event burnout in power diodes is investigated primarily with simulated temporal electrical characteristics.

First, the structure of a diode and its electrical characteristics under different operating modes are discussed [19]. The electrical characteristics of a diode are explained in depth with device physics concepts. It is necessary to understand the physics of a diode under different operating modes.

Structure of a diode

Essentially, a diode has a single *pn* junction that is formed when p-type and n-type semiconductors are joined physically. A p-type semiconductor with excess holes is obtained by addition of acceptor impurity ions, while an n-type semiconductor with excess electrons is formed by addition of donor impurity ions. A typical structure of a diode is shown in Figure 3. Here, a *pn* junction is formed between diffused p-type (p^+) and epitaxial n-type (n^-) regions. The plus (+) and minus (-) signs represent heavily and lightly doped semiconductors respectively. High conductivity is necessary near a metal contact to form an Ohmic contact. Lightly doped semiconductors have low conductivity.

Therefore, a heavily doped n-type semiconductor (n^+) having high conductivity is created to form an ohmic contact for the n-region of a diode.
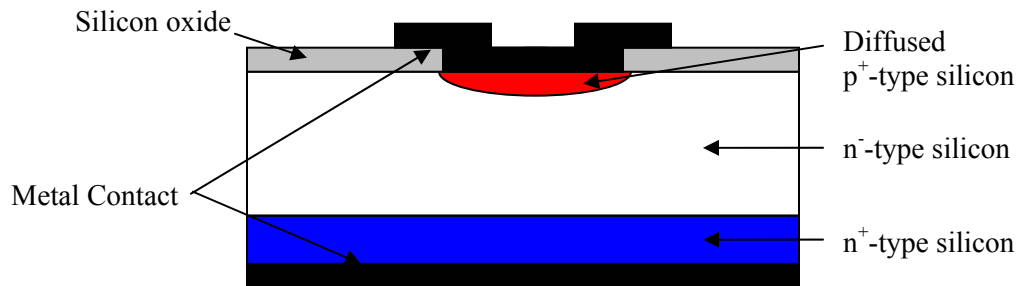
Figure 3 Structure of a diode.

Two simple models of *pn* junctions are the *step junction* and the *graded junction*. In a *step junction*, uniformly doped p-type and n-type regions are separated by a sharp junction. In the case of a *graded junction*, the transition from a p-type semiconductor to an n-type semiconductor occurs over a significant distance. *Step junctions* can be used to represent epitaxial junctions, while a *graded junction* is a reasonable approximation of a diffused junction. All the fundamental concepts of *pn* junction theory are similar for step and graded junctions. The *step junction* is primarily used to explain the *pn* junction theory because it represents the simplest mathematical model. The same theory with appropriate corrections is applied for *graded junctions*. Basic concepts of the *pn*-junction theory are explained for *step junctions* in the present work.

Basic Device Characteristics

A diode can be operated in two modes, *forward* and *reverse*. The performance of a diode under the forward and reverse operating modes is determined by forward and reverse

electrical characteristics respectively. First, a diode under equilibrium conditions is discussed. Next, forward and reverse characteristics are explained with the support of device physics.

Diode at Thermal Equilibrium

n- and *p*-type semiconductors have a large concentration of free electrons and holes, respectively. Both the semiconductors are neutral in the bulk region. One carrier is present for each ionized impurity atom in the bulk semiconductor material. Electrons from the n-type semiconductor diffuse into the p-type semiconductor due to a significant difference in electron concentration. The reduced electron concentration leaves behind positive impurity ions near the junction. Likewise, negative impurity ions are left near the junction when holes from p-type material diffuse across the junction to n-type material. Thus, a *space charge* region is developed near the metallurgical junction, where positive impurity ions are on the n-side of the junction and negative impurity ions are on the p-side of the junction. This region is also called the *depletion region* because of the low number of free electrons and holes. An electric field, E, is created in the depletion region and a *potential barrier* is formed. The direction of the electric field is opposite the diffusion current. The electrons and holes diffuse across the junction until the magnitude of the electric field is increased to the level where electrons and holes have insufficient energy to overcome this barrier. The resulting potential difference is called the *built-in voltage*, ϕ_i, and no net current flows across the junction. The *pn* junction is said to be in thermal equilibrium at this point as shown in Figure 4.
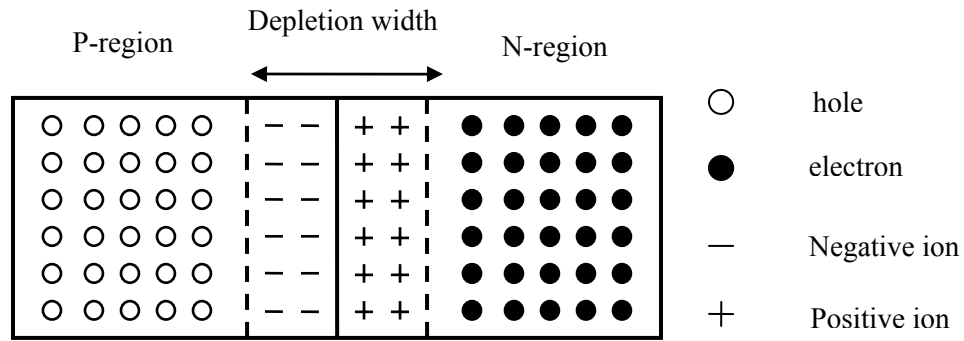
Figure 4 *pn* junction at thermal equilibrium.

The energy band diagram of a *pn* junction is sketched in Figure 5. Here E_c represents the conduction band edge, E_v represents the valence band edge, and E_{fn} and E_{fp} represent the Fermi levels of the n- and p-type semiconductors, respectively.
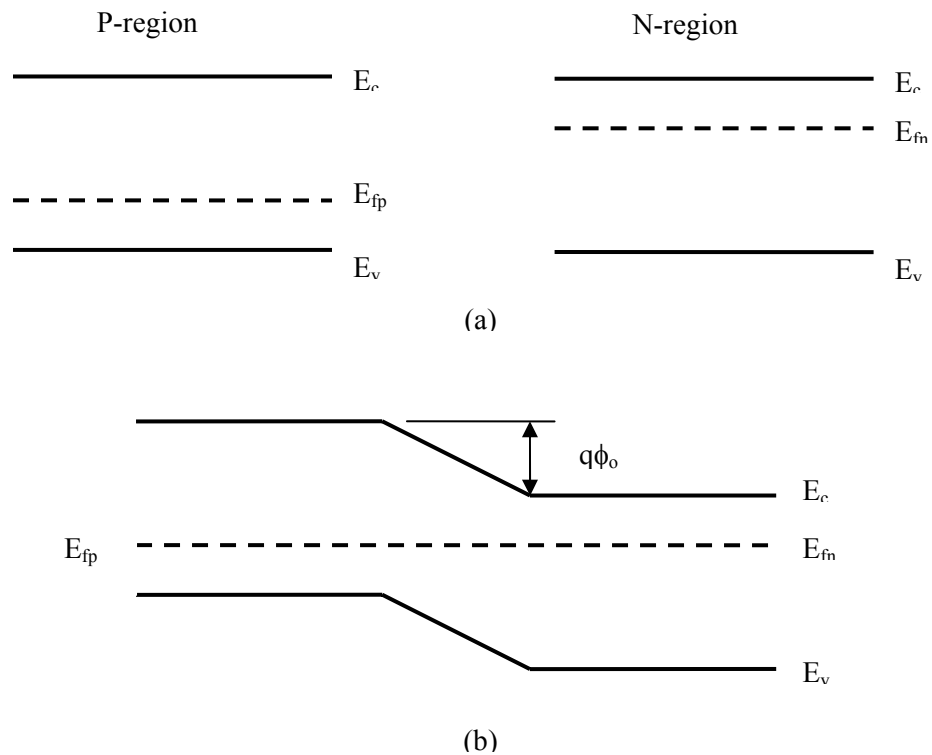
Figure 5 Band diagrams showing formation of a *pn* junction.

The built-in voltage of a *pn* junction depends on donor atom concentration, N_d in the n-region and acceptor atom concentration, N_a in the p-region, which can be calculated analytically from the following equation [19].

$$\phi_i = \frac{\kappa_B T}{q} \ln\left(\frac{N_a \times N_d}{n_i^{2}}\right) \tag{1}$$

where κ_B is Boltzmann's constant, q is the charge of an electron, T is temperature and n_i is the intrinsic carrier concentration. The depletion region width, X_d, is analytically calculated by the following equation, where ε_s is the permittivity of the semiconductor.

$$X_d = \left[2\frac{\varepsilon_s}{q} \phi_i \left(\frac{1}{N_a} + \frac{1}{N_d} \right) \right]^{\frac{1}{2}} \tag{2}$$

<u>Forward Bias Condition</u>

A *pn* junction operates in the forward mode when positive bias is applied to the p-region with respect to n-region. The majority carriers in each region move towards the junction and neutralize some of the space charge as seen in Figure 6. The depletion width is reduced and the potential barrier is lowered during the forward bias mode causing a decrease in resistance to the current flow across the junction. The electrons from the n-region overcome the barrier and enter the p-region where they recombine with holes. Similarly, holes from the p-region cross the barrier and enter the n-region where they recombine with electrons.
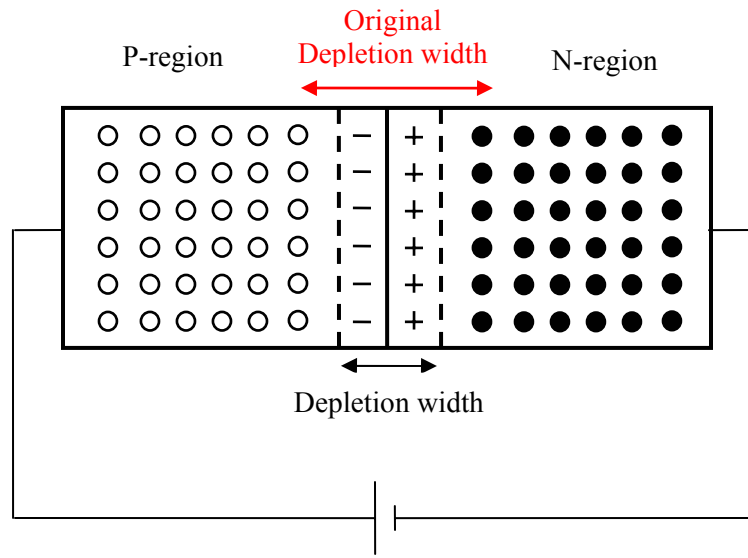
Figure 6 Forward biased *pn* junction.

In forward bias, the current across the junction increases as positive bias is applied to the p-region. Figure 7 shows typical forward bias characteristics.
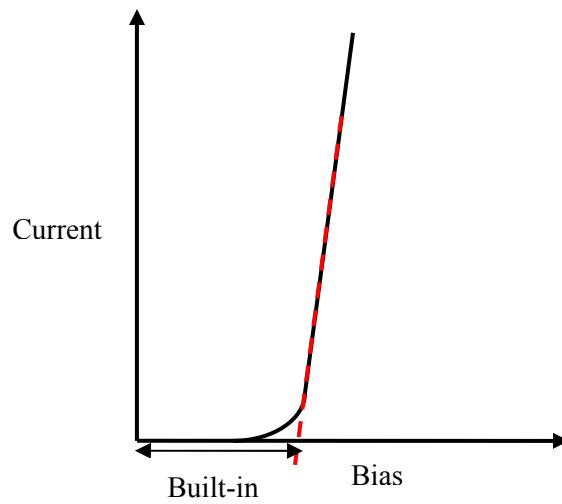
Figure 7 Forward bias characteristics of a diode.

Reverse Bias Condition

The reverse bias condition is achieved when negative voltage is applied to the p-region with respect to the n-region as seen in Figure 8. The majority carriers in each region are attracted away from the junction by the contacts. This leads to increased depletion width and higher potential barrier, which prevents flow of current across the junction due to majority carriers. However, a small current flows across the junction due to the flow of minority carriers across the junction under the applied bias.
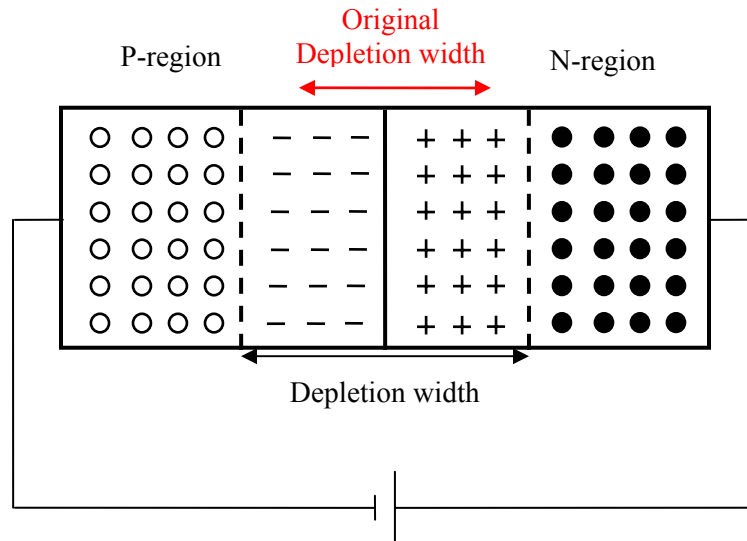
Figure 8 Reverse biased *pn* junction.

The current across the junction is plotted as a function of reverse bias in Figure 9. One important feature of the reverse bias characteristics is the *breakdown voltage*, the voltage above which a diode conducts high current in the reverse mode.
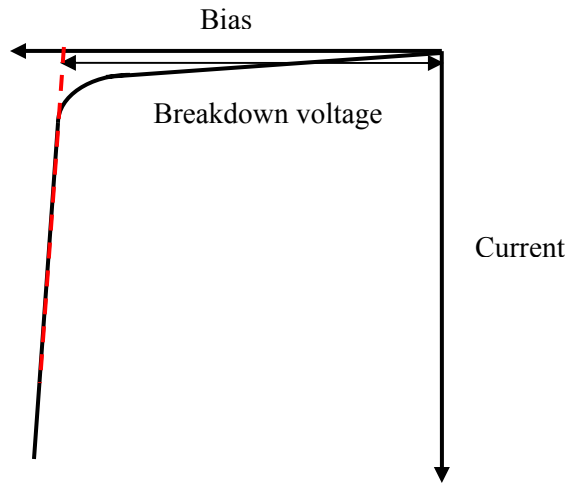
Figure 9 Reverse bias characteristics of a diode.

CHAPTER III

CHARGE AND ENERGY TRANSPORT IN SEMICONDUCTORS

The Schrödinger wave equation is the most accurate way of explaining the motion of the charge carriers in semiconductors. However, obtaining the device characteristics with wave theory is extremely tedious. The wave theory concept needs to be applied when the carrier transport in the nanoscale semiconductors is considered. Transport theories are utilized to solve for the carrier transport in microscale devices, which consider the carriers as particles possessing related properties such as mass, momentum and energy.

Drift-Diffusion Model

The drift-diffusion model is predominantly used to describe the transport of charge carriers (electrons and holes) in semiconductor devices. The drift-diffusion model is formulated with the conservation of particle density and momentum balance, but the energy balance model is neglected. The temperature of the carriers is assumed to be that of the lattice temperature, which is usually set as ambient temperature. Thus, the effect of temperature on device parameters is not incorporated when the drift-diffusion model is used solely. However, the lattice energy equation can be solved self-consistently with the drift-diffusion model to include the temperature dependence of device properties.

Poisson's Equation

The spatial variation of charge density encountered within the semiconductor devices leads to spatial variation of potentials. Poisson's equation relates the electric field and electrostatic potential to the local charge density:

$$\nabla \cdot (\nabla \psi) = -\frac{q}{\varepsilon_s}(p - n + N^+{}_d - N^-{}_a),$$

(3)

where ε_s is the electrical permittivity of the semiconductor and ψ is the electrostatic potential. p and n represent the hole and electron concentrations, respectively, while $N^+{}_d$ and $N^-{}_a$ denote the concentration of the ionized donor and acceptor atoms, respectively.

Carrier Continuity Equations

The carrier continuity equation describes the change in the carrier concentration over time in an infinitesimally small volume within a semiconductor considering various mechanisms that affect carrier density. The continuity equations for electrons and holes are given as:

$$\frac{\partial n}{\partial t} = \frac{1}{q}(\nabla \cdot \vec{J_n}) + G_n - R_n$$

(4)

$$\frac{\partial p}{\partial t} = -\frac{1}{q}(\nabla \cdot \vec{J_p}) + G_p - R_p$$

(5)

where $\vec{J}$ represent current density, and G and R denote generation and recombination rates. In the above equations the subscripts n and p are used for the electrons and holes, respectively.

Current Equations

The current density relations for electrons and holes are given as [20]:

18

$$\vec{J_n} = qD_n\nabla n + qn\left\{\mu_n\nabla\left(-\psi + \frac{E_c}{q}\right) + D_n\nabla T_n - \frac{3}{2}D_n\nabla\ln(m_n)\right\} \tag{6}$$

$$\vec{J_p} = -qD_p\nabla p + qp\left\{\mu_p\nabla\left(-\psi + \frac{E_v}{q}\right) + D_p\nabla T_p - \frac{3}{2}D_p\nabla\ln(m_p)\right\} \tag{7}$$

The first term on the right hand side is current due to diffusion of carriers; the second term includes current flow under the influence of electric field. Current flow due to spatial variation of carrier temperature is described by the third term. The last term accounts for the current flow due to variation in bandgap. The above current relations include position-dependent band energies, E_c and E_v, and position-dependent effective masses, m_n and m_p for electrons and holes. D_n and D_p are the diffusion coefficients for electrons and holes. T_n and T_p are the carrier temperatures that are assumed to be equal to the lattice temperature T_L in the drift-diffusion model. μ_n and μ_p are the electron and hole mobility values. The concept of mobility will be introduced later in this chapter.

In the drift-diffusion model, a non-degenerate equilibrium distribution function is assumed, i.e., the Fermi energy is at least $3k_BT$ below or above the conduction or valence band edge, respectively. The temperature inside the entire device is constant unless the external lattice energy equation is solved to determine the actual temperature distribution within the device.

Lattice Energy Model

Temperature-dependent device properties can be determined when the lattice energy model is coupled with the drift-diffusion model. Self-heating effects are incorporated in this model by solving the lattice heat flow equation self-consistently with the drift-diffusion transport model. The lattice energy equation is given by [20]:

$$\rho C \frac{\partial T}{\partial t} = \nabla \cdot (k \nabla T) + (\overrightarrow{J_n} + \overrightarrow{J_p}) \cdot \vec{E} + RE_g \tag{8}$$

In the above equation, ρ is density; C is heat capacity; k is the thermal conductivity, R denotes carrier recombination rate, and E_g is the band gap of the semiconductor.

This model includes three heat source terms: Joule heating is represented by the second term on the right hand side, while the third term represents heating due to carrier recombination. As the strong two-way coupling is maintained between the lattice energy and drift-diffusion models, effects of device behavior on temperature and temperature on device properties are included. Note that the other temperature-dependent models such as mobility and impact ionization are required to get the most accurate results.

In the present work, the drift-diffusion model is used in conjunction with the lattice energy model.

Carrier Movement in Semiconductors

Motion of carriers in a semiconductor at thermal equilibrium is completely random so that no net current flows. A non-equilibrium condition exists when an external field is applied. Carrier motion in this case is *carrier drift*. Non-equilibrium is also induced when a large number of carriers (electron-hole pairs) are created in a local region of a semiconductor, for example, following an ion strike. Carrier movement under the influence of a concentration gradient is known as *carrier diffusion*. Both the mechanisms are explained briefly below [19].

Carrier Drift

Movement of carriers under the influence of electric field is controlled by the direction of field and polarity of the carriers. Electrons move in the opposite direction of applied field, while holes move in the same direction. A proportionality factor, µ, known as *mobility* describes how freely carriers move under the influence of an electric field. The drift velocities for electrons and holes are given by:

$$\vec{\upsilon}_n = -\mu_n \cdot \vec{E} \; ; \tag{9}$$

$$\vec{\upsilon}_p = \mu_p \cdot \vec{E} \; , \tag{10}$$

where drift velocities ($\vec{\upsilon}_n$ and $\vec{\upsilon}_p$), carrier mobility values (μ_n and μ_p) are denoted for electrons and holes respectively, while $\vec{E}$ represents electric field.

Carriers moving in the semiconductor collide with the lattice, ionized impurity atoms, free carriers, and other scattering centers. Therefore, the mobility of carriers is governed by various scattering mechanisms. Scattering of the carriers with the thermally generated lattice vibrations is termed *lattice scattering*. Lattice scattering increases as the temperature is increased because of increased thermally-generated vibrations. Interaction of the carriers with ionized impurity atoms results in *impurity scattering*. *Carrier-carrier scattering* is an interaction between the mobile carriers (electrons and holes), which serves to restore equilibrium.

Linear dependence of drift velocity on electric field is valid when the velocity imparted to a carrier by the field is much less than the thermal velocity. At high electric fields, velocity imparted to the carriers is comparable to the thermal velocity of the carriers and

the above assumption is invalid. The drift velocity saturates at high electric fields and is called the saturation velocity, v_{sat}. At 300 K, the saturation velocity for electrons is 1.07×10^7 cm/s and for holes is 8.34×10^6 cm/s [21]. The saturation velocity decreases with an increase in temperature.

Temperature-dependent mobility

Scattering mechanisms that affect the carrier mobility have varying temperature dependencies. Impurity scattering becomes less effective at high temperature because high velocity carriers interact less effectively with impurity atoms. The lattice scattering becomes dominant at high temperature due to the increased lattice vibrations that scatter the carriers. Thus, mobility increases at low temperatures where the impurity scattering is dominant, while it decreases at high temperatures where the lattice scattering is dominant.

The drift current densities for electrons and holes are given as:

$$\vec{J}_{n,drift} = nq\mu_n \vec{E} \tag{11}$$

$$\vec{J}_{p,drift} = pq\mu_p \vec{E}. \tag{12}$$

Carrier Diffusion

Spatial variation of carrier densities in a semiconductor gives rise to diffusion current. The diffusion current densities of electrons and holes are calculated by the following equations:

$$\vec{J}_{n,diffusion} = qD_n \frac{dn}{dx} \tag{13}$$

$$\vec{J}_{p,diffusion} = -qD_p \frac{dp}{dx} \tag{14}$$

In the above equations, D_n represents the *diffusion constant* for electrons and D_p represents the *diffusion constant* for holes. The diffusion constant describes carrier diffusion, while mobility characterizes carrier drift in semiconductors. These two constants are related to each other by the *Einstein relation*:

$$D_{n,p} = \left(\frac{k_B T}{q} \right) \mu_{n,p} . \tag{15}$$

Excess Carriers in Semiconductors

Most semiconductor devices during normal operation are subjected to non-equilibrium conditions. A non-equilibrium condition exists when carriers in excess of the thermal equilibrium value are created. Excess carriers are created under various conditions such as forward biased junctions, high electric fields in reverse-biased junctions, incidence of photons, and passage of ionizing particles. If the perturbation that creates excess carriers is removed, the excess carriers are removed over time and equilibrium is restored.

Recombination

The *mass action law* governs the equilibrium concentration of carriers given by $pn = n_i^2$. Recombination is the process in which excess carriers (electron-hole pairs) are annihilated. Thus, recombination restores the equilibrium condition where non-equilibrium may exist ($pn > n_i^2$). The average time required for an electron-hole pair to recombine is called *recombination lifetime*, τ_r.

Recombination mechanisms that are dominant in semiconductors are classified as band-to-band recombination (direct recombination), trap-assisted recombination (indirect recombination), and Auger recombination. The direct recombination is dominant in direct band gap semiconductors such as GaAs, but unlikely in indirect band gap semiconductors such as Si. The recombination occurs in the bulk as well as at the surface.

Shockley-Read-Hall Recombination

Shockley-Read-Hall (SRH) recombination is a non-radiative mechanism that is prevalent in indirect semiconductors. Schematic of SRH recombination is shown in Figure 10. Electrons from conduction band (E_c) and holes from valance band (E_v) recombine via 'deep' level defects. The defect density N_T is characterized by energy E_T. The energy level E_T lies in the middle of the band gap for 'deep' defect levels. An electron from the conduction band and a hole from the valence band meet at the trap level and an electron-hole pair is cancelled out. Energy liberated during the recombination is produced as lattice vibrations (phonons). Therefore, SRH recombination is characterized as a non-radiative mechanism.
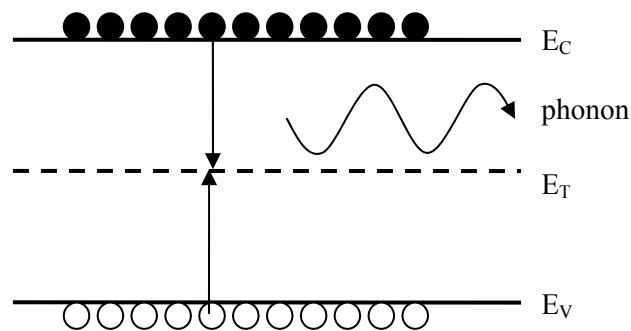
Figure 10 Shockley-Read-Hall recombination process in a semiconductor.

SRH recombination is measured by the recombination rate R_{SRH}, i.e., the number of electron-hole pairs recombined per unit volume per unit time. The recombination rate R_{SRH} is given by:

$$R_{SRH} = \frac{np - n_{ie}^2}{\tau_p(n + n_1) + \tau_n(p + p_1)},$$ (16)

$$n_1 = n_{ie}e^{(E_T - E_i)/k_BT}; \quad p_1 = n_{ie}e^{(E_i - E_T)/k_BT},$$

where n, p are total carrier densities, i.e., the sum of the equilibrium and excess carrier densities, τ_p, τ_n are the recombination lifetimes for holes and electrons, n_{ie} denotes effective intrinsic carrier concentration that accounts for temperature dependence, E_i denotes intrinsic energy level and E_T is trap energy level.

Auger Recombination

Auger recombination involves the interaction of three particles, i.e., two electrons and a hole or two holes and an electron. When an electron in the conduction band recombines with a hole in the valence band, the released energy is absorbed by another carrier and the momentum in this process is also conserved. The energy and momentum is gained by an electron in n-type semiconductors and a hole in p-type semiconductor. Figure 11 depicts Auger recombination in n-type semiconductors. This is also a non-radiative recombination process. Auger recombination is significant in high injection conditions and regions of high doping concentrations (carrier concentrations $> 10^{19}$ cm^{-3}). Therefore it is important in power diodes as the regions near the contacts are heavily doped.

Auger recombination rate R_{Auger} is given by:

$$R_{Auger} = \left(C_n^{Auger} \cdot n + C_p^{Auger} \cdot p\right)\left(pn - n_{ie}^2\right),$$ (17)

where at 300 K, $C_n^{Auger} = 2.8 \times 10^{-31}$ cm^6/s and $C_p^{Auger} = 9.9 \times 10^{-32}$ cm^6/s [22].
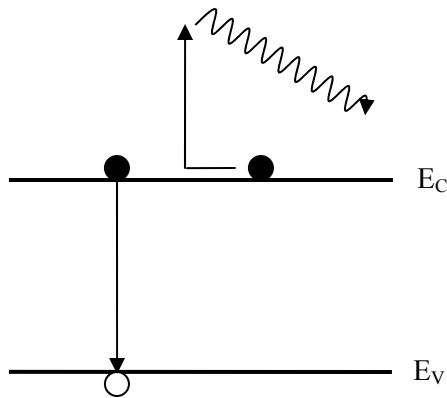
Figure 11 Auger recombination process in a semiconductor.

Temperature-dependence of Intrinsic Carrier Concentration

The intrinsic carrier concentration (n_i) is a strong function of the temperature:

$$n_i{}^2 = N_C N_V \exp\left(\frac{-E_g}{k_B T}\right), .$$ (18)

In the above equation, N_C and N_V are the effective densities of states at the conduction-band and valence-band edges, respectively. The intrinsic carrier concentration has exponential temperature dependence, which is very important. The effective densities of states and band gap are weak functions of temperature.

In extrinsic semiconductors, the carrier concentration is controlled by the impurity concentration because the intrinsic carrier concentration is much less than the majority carrier concentration ($n_i \ll n$ in n-type and $n_i \ll p$ in p-type semiconductors). However, if the temperature rise is sufficient, the intrinsic carrier concentration can be comparable to the impurity concentration. If the intrinsic carrier concentration is comparable to or greater than the impurity concentration in an extrinsic semiconductor, then the

temperature, instead of impurity concentration, controls the carrier concentration in extrinsic semiconductors.

The power diode structure used in the present work has the base doping level of 3.2×10^{13} cm^{-3}. The analytical calculation predicts that the intrinsic carrier concentration around 440 K is comparable to the base doping concentration. The temperature where the intrinsic concentration approaches the doping level will be called the intrinsic temperature.

Generation

Generation of carriers in a device leads to non-equilibrium conditions. Carrier generation is attributed to various mechanisms such as impact ionization, photon absorption, and passage of fast charged particles through a device. Carrier generation due to impact ionization and ion strikes is explained in depth because these are the modes of carrier generation in the present power diode study.

Impact Ionization

Reverse biased *pn* junctions are subjected to high electric fields because the applied voltage drop occurs completely within the depletion region. The electric field increases as the reverse bias on a junction is increased. Free carriers within the depletion region are accelerated under the influence of high electric fields (above 1×10^5 V/cm). Thus, the carriers gain high kinetic energies and attain high velocities ($\sim 1 \times 10^7$ cm/s). When a high energy carrier collides with the lattice, it can cause an electron from the valence band to be transferred to the conduction band, creating an electron-hole pair. The ionization

process initiated with the impact of an energetic carrier is called *impact ionization*. *Impact ionization* process is described with a band diagram in Figure 12.
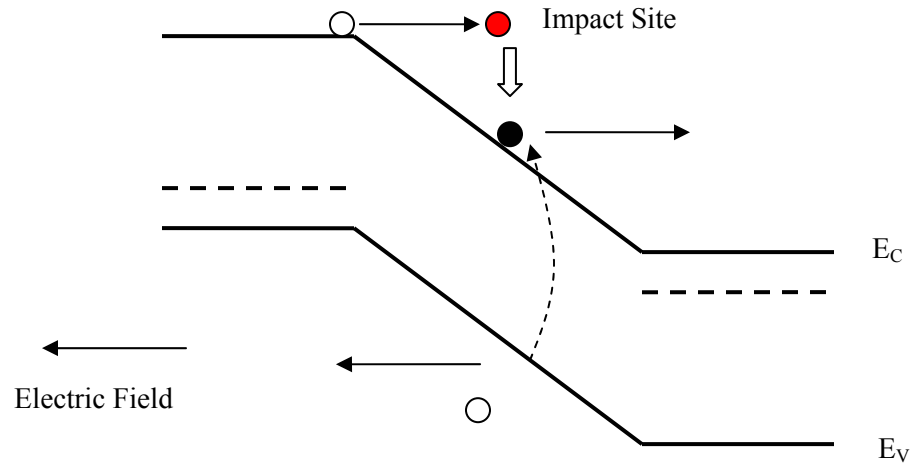
Figure 12 Impact ionization

The electron-hole pairs created by impact ionization are also accelerated in the high electric fields, thus gaining high energies and velocities. These carriers collide and create more electron-hole pairs by impact ionization. The multiplicative behavior of the impact ionization mechanism continues further and generates more electron-hole pairs. Increased carrier density in the depletion region produces high current across the junction. Ionization rate is a measure of electron-hole pairs created. *The avalanche breakdown voltage* of a reverse biased *pn* junction is defined as the voltage where the ionization rate approaches infinity. Power diodes are operated at high reverse bias voltages so impact ionization is significant.

The *ionization coefficient* is described as the number of electron-hole pairs created per unit distance traveled. The carriers gain more energy when the electric field is higher,

thus ionization rate is a function of electric field and position. The ionization coefficient is at a maximum where the peak electric field occurs. The electric field dependence of ionization coefficient for silicon is given by

$$\alpha_i(E) = \alpha_i^{\infty} \exp\left[-\left(\frac{E_i^{crit} \cdot |J_i|}{E \cdot J_i}\right)\right]_{,i=n,p} ,$$

(19)

where E_i^{crit} is critical electric field for impact ionization and α_i^{∞} is ionization constant. Values of the constants for electrons and holes are: $E_n^{crit} = 1.75 \times 10^6$ V/cm, $\alpha_n^{\infty} = 3.8 \times 10^6$ cm^{-1}, $E_p^{crit} = 3.26 \times 10^6$ V/cm and $\alpha_p^{\infty} = 2.25 \times 10^7$ cm^{-1}.

The carrier generation rate G denotes the number of carriers generated per unit volume per unit time. The carrier generation due to impact ionization is expressed as

$$G = \alpha_n J_n + \alpha_p J_p = \alpha_n n \upsilon_n + \alpha_p p \upsilon_p ,$$

(20)

where J_n and J_p are the current density for electrons and holes, respectively. The current density can be specified in terms of carrier velocities (υ_n and υ_p) and carrier densities (n and p). The ionization coefficients for electrons and holes (α_n and α_p) are described earlier.

Ion strike induced carriers

An energetic ionizing particle passing through materials deposits energy along its path. Linear energy transfer (LET) describes the energy deposited by the particle per unit length traveled in the target material. LET is target material-dependent and is usually described in MeV-cm^2/mg. Ionization energy, the energy required to create an electron-hole pair, for a semiconductor is a characteristic property. For silicon, an average of 3.6 eV is required to create an electron-hole pair [23]. When the energy deposited by a particle in a semiconductor exceeds the ionization energy, electron-hole pairs are created

along its path. The number of created electron-hole pairs is calculated based on the deposited energy and ionization energy for the material.

In the ion-strike model, generated carriers are deposited uniformly in a cylindrical column of a specified radius. The overall carrier generation term due to an ion strike is calculated as:

$$G(l,r,t) = f(l,r) \cdot g(t) \tag{21}$$

The first term on the right side is the spatial term, while the second term is the temporal term. The LET is included in the spatial term. Introduction of strike-induced carriers is modeled as Gaussian in time. Although the normal transit time of an ion through a device is in the range of femtoseconds, the distribution of induced carriers in the picoseconds regime is used for simulation stability without the loss of long term accuracy.

CHAPTER IV

SIMULATIONS AND RESULTS

Device-level simulations were performed in the present study of single-event burnout in power diodes and comparisons were made to measurements in the literature. Voss et al. experimentally observed single-event burnout in power diodes for high energy C^{12} ions [13]. A diode that failed due to normal incidence of C^{12} ion possessing 252 MeV energy was selected to study the burnout mechanism in power diodes. CFD-Semi-Device simulations tools developed by CFD Research Corporation were used for the present work.

3-D simulations require significantly more computation power compared to 2-D simulations. In this work, a 2-D diode rectangular structure was used for simulations. Not all device details necessary for modeling the diode are reported in the literature. The device geometry and breakdown voltage of the diode are reported, but doping concentrations are not specified. Therefore, approximations were made for features such as doping profiles in the simulated diode structure.

Diode Structure

A 2-dimensional p^+-n^--n^+ diode structure was created with p^+-region width of 100 μm, n^-- region (base) width of 450 μm, and n^+-region width of 25 μm [13]. The breakdown voltage of the diode was specified as 4500 V. Because the base-region doping

concentration primarily governs breakdown characteristics of diode, a base-region doping concentration of 3.2×10^{13} cm^{-3} was determined for the breakdown voltage of 4500 V. The doping concentrations of p^+- and n^+- regions modify the forward-bias characteristics of the diode, but not the breakdown voltage. As diode burnout is observed during reverse-bias operation, the p^+- and n^+- region doping concentration approximations are valid and do not affect the burnout mechanism. p^+- and n^+- region doping concentrations were set as 1×10^{19} cm^{-3}. An abrupt doping profile was used at the p^+-n^- junction, while a Gaussian profile was used at the n^--n^+ junction to avoid sharp potential drop. The simulated diode structure is shown in Figure 13.
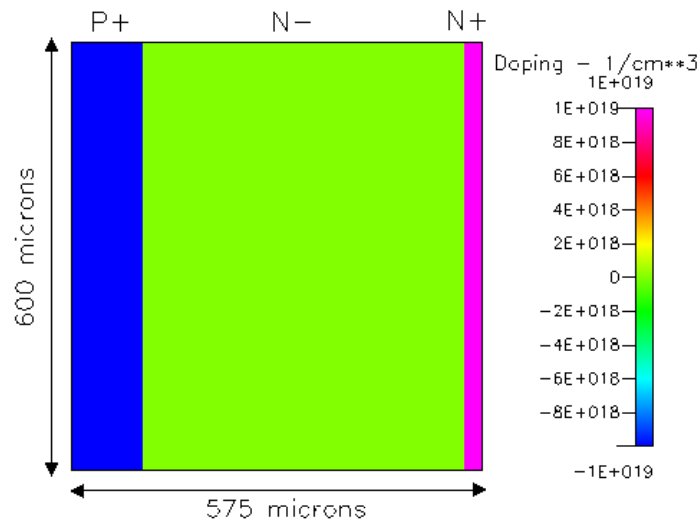

Figure 13 Simulated diode structure showing doping

Device Implementation and Simulation Methodology

CFD-GEOM, the structure modeling and mesh generation tool, was used to create a 2-D diode model of required dimensions. A structured discretization technique was employed to divide the diode structure into finite elements for computations. A total of 28000 nodes

with a non-uniform distribution were created inside the diode. Very small elements are required in the regions where large gradients are anticipated. Thus, a very fine mesh was generated near the *pn* junction and along the ion track through the diode where high doping and electric field gradients are expected. The discretized structure is shown in Figure 14. It is important to discretize the structure into elements that produce a fully converged solution. Convergence was confirmed by refining the mesh until computed quantities no longer changed with this mesh. Doping profiles for the structure are specified in a text format. Doping concentration and roll-off distances along two coordinate axes for each region are defined in the doping file format.

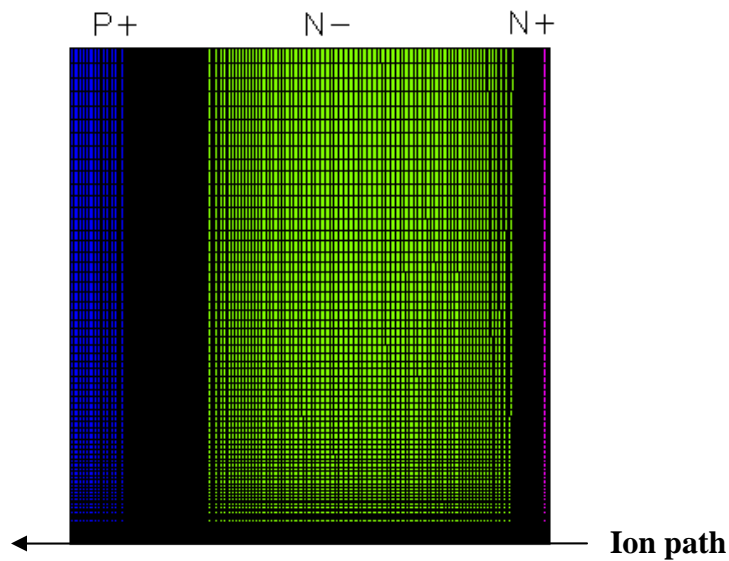Figure 14 Diode structure showing refined mesh near junctions and along ion path.

CFD-ACE+ is a graphical user interface that is used to set-up device models and specify solution parameters. CFD-Semi-Device and Heat modules are selected for all semiconductor device simulations. The drift-diffusion model is employed in the present work. The impact ionization model, which is critical in power device simulations, is

selected because large electric field gradients are encountered. In a few simulations in the present work, the impact ionization model was excluded to isolate the effect of avalanche-generated charge. The ion strike model is included in all transient simulations, where effects of ion strike are simulated. Ion strike parameters such as angle of incidence, strike-induced track radius, Linear Energy Transfer (LET) are specified in this model. All of the simulated ion strikes were at normal incidence. The electron-hole pair creation energy in Si is 3.6 eV/e-h pair, which is used to convert energy to charge density. Newton's fully coupled iterative algorithm is utilized to obtain direct solutions to all semiconductor equations.

The LICE mobility model that includes effects of lattice, impurity, carrier-carrier scattering along with field-dependent mobility is employed. A constant carrier lifetime of 10 μsec is used for electrons and holes. The thermal conductivity of silicon is 1.5 W/cm-K and the specific heat is 0.7 J/g-K [24]. The electrical and thermal boundary conditions for diode simulations are shown in Figure 15. Ohmic contacts to the p^+ and n^+ regions assure zero potential drop across them. For all the simulations, the temperatures at external boundaries were fixed at 300 K unless otherwise specified. Carrier and heat flow across the symmetry boundary (strike location) is zero, where the axis of symmetry is a zero flux boundary.

Insulator, isothermal

P+   N−   N+

Ohmic. isothermal

Ohmic. isothermal

Strike
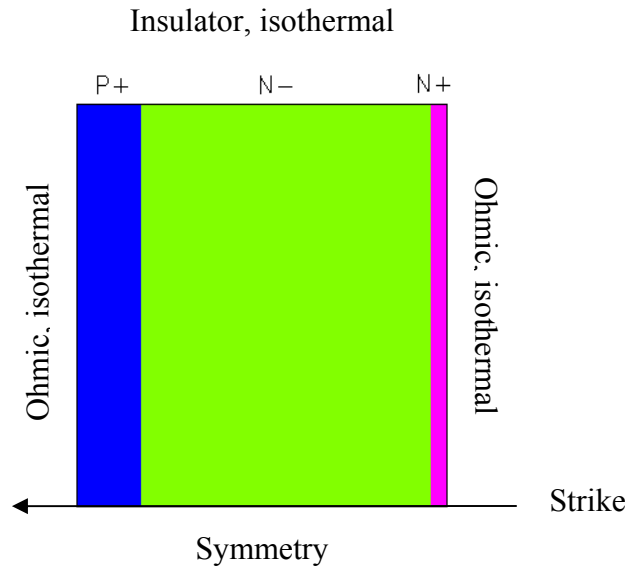
Symmetry

Figure 15 Diode structure showing boundary conditions. Symmetry condition indicates no carrier and heat flow across the boundary.

Isothermal simulations (thermal model OFF) assume a default uniform temperature of 300 K inside the device. The values of all temperature-dependent parameters at 300 K are used in these simulations. Isothermal simulations at different temperature can be performed by specifying the temperature at all isothermal boundaries. Temperature-dependent parameters at the specified temperature are used in each specific simulation. In non-isothermal simulations (thermal model ON), the lattice heat equation calculates localized temperatures that are used to determine locally temperature-dependent parameters. As the drift-diffusion equation is solved self-consistently with the lattice heat equation, localized temperature effects are reflected in device characteristics.

Steady-state Simulations

The I-V characteristics of the diode were obtained from steady-state simulations. These characteristics were simulated using the drift-diffusion model combined with lattice heat equation. The potential drop across the p^+-n^- junction can be calculated analytically. Potential drop across only the p^+-n^- junction in the simulated structure is acquired by plotting potential inside the diode at different locations, which is shown in Figure 16. The potential drop across the p^+-n^- junction (0.72 V) obtained from the simulated structure is in agreement with analytically calculated voltage drop (0.74 V).
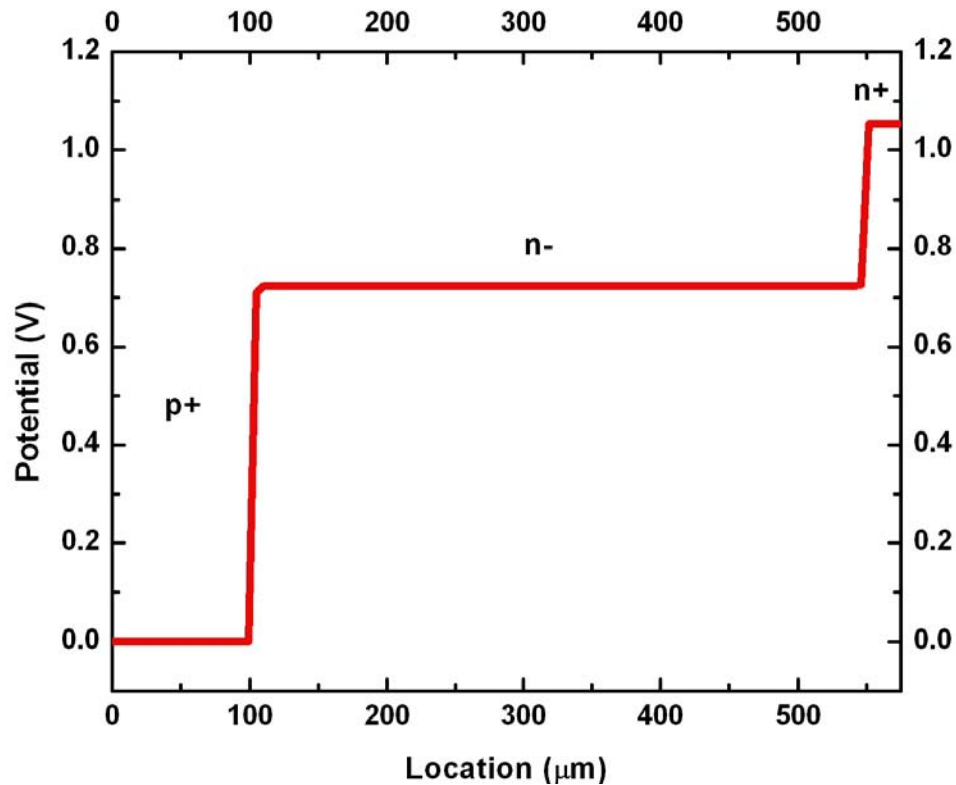
Figure 16 Built-in potential across the diode at equilibrium.

Reverse-bias characteristics were obtained when the bias on the p^+ contact was decreased from 0 V to - 5000 V in steps while the n^+ contact was grounded. Impact ionization was included in the simulation. Figure 17 shows the reverse bias characteristics of the diode. Simulated breakdown voltage (- 4500 V) is in relatively good agreement with the analytically calculated breakdown voltage (-4850 V). The maximum electric field at breakdown (E_{max}) of 2.096×10^5 V/cm attained in the simulated structure agrees well with the analytical maximum field of 2.18×10^5 V/cm. The basic diode parameters obtained for the simulated structure are in agreement with the analytically obtained parameter values. This confirms that the diode structure is modeled accurately.

Figure 17 Simulated reverse bias characteristics for the power diode structure

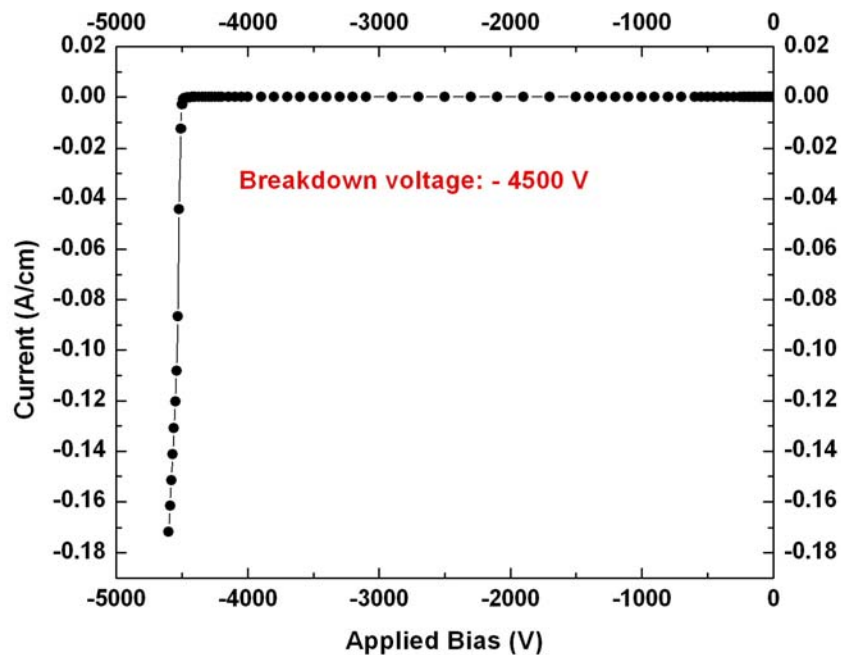## Transient Simulations

Single-event burnout is a transient process. Current flowing through the diode following the strike was simulated as a function of time. All ion-strike simulations performed hereafter involve current flowing through the diode following the strike.

The single-event burnout simulations described here are conducted for a C^{12} ion possessing energy of 252 MeV. SRIM [25] simulations were used to calculate the ion range. The energy loss per unit length along its path does not vary significantly. Therefore the assumption of uniform carrier density along the ion path is valid. The linear energy transfer of a 252 MeV C^{12} ion is estimated as 0.71 MeV-cm^2/mg [26]. The charge filament is formed as a cylindrical column of uniform density. The radial distribution of generated charge is approximated as a step function and the ion is assumed to pass all the way through the device. The distribution of radial energy around the track in silicon is reported by Fageeha et al. for C^{12} ions with energies of 15 MeV and 100 MeV [27]. Charge density inside the ion-track in the diode is estimated for 252 MeV C^{12} ions from the radial dose distribution function. The same charge density is simulated inside the cylindrical column. With such approximations, an ion track of 0.15 μm radius is modeled for the chosen ion.

An ion strike is inherently 3D in nature. For symmetric structures, the 3D nature of the ion-strike can be simulated with 2D axi-symmetric simulations. In the present work, 2D rectangular simulations are performed due to limitations of the simulation tools. However, 2D rectangular simulations are capable of capturing physical mechanisms

qualitatively. 2D axi-symmetric simulations simulate a cylindrical diode, while 2D rectangular simulations simulate rectangular parallelepiped diodes. Carrier density inside the track for a given LET value is determined assuming cylindrical track structure of specified radius. The ion track in 2-D rectangular coordinate simulations is represented by a sheet of charge, where the track diameter is the thickness of the charge sheet. The same carrier density is maintained in the charge sheet in 2-D simulations. Schematic of the track structure in 2-D simulations is shown in Figure 18. Note that the problem is symmetric about the plane as shown in Figure 18. The diode is simulated only above the plane of symmetry, with the ion-strike along the plane of symmetry. This reduced dimensionality is utilized for computational simplicity. For 2D rectangular simulations, the depth of the device in the third dimension is considered to be 1 cm. There are no gradients along the depth of diode. Therefore current is always reported per centimeter for 2D rectangular simulations.
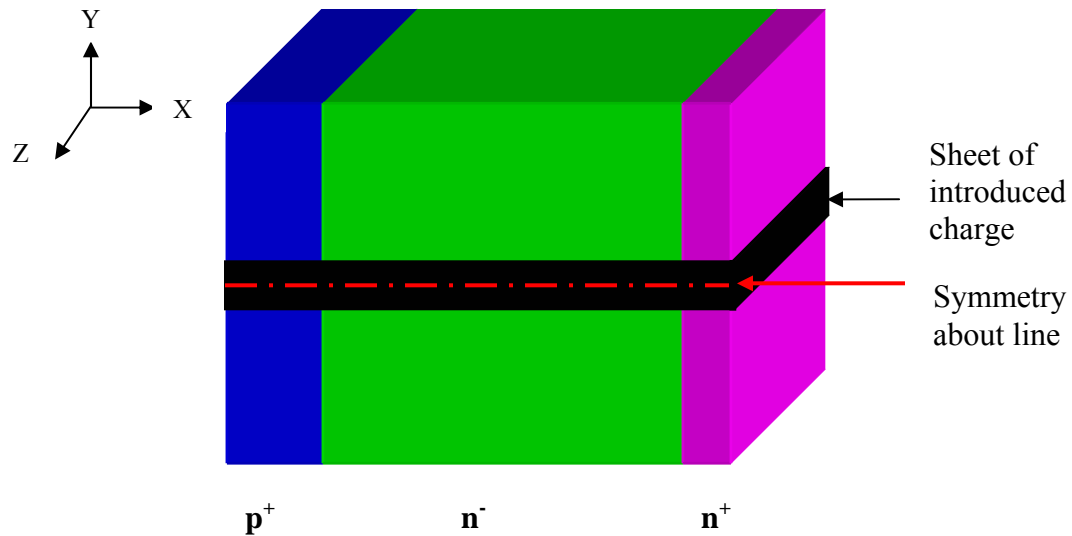

Figure 18 Schematic of track structure modeled in 2-D ion-strike simulations.

The charge is deposited at the center of the cylindrical diode along its length. The diffusion of the charge deposited during the ion strike is isotropic in nature. The charge diffusion is identical in all radial directions. In the case of the 2D rectangular structure, the charge sheet is introduced along the x-z plane. The gradients due to charge diffusion are solely along the y-coordinate and not along the depth of the diode (z-coordinate).

<u>Effect of an ion strike on diode current</u>

Single-event burnout is observed only in reverse-biased diodes. The reverse-biased diode does not conduct current prior to the ion strike, except for the reverse leakage current. When an ion strikes a diode, the deposited energy generates electron-hole pairs in the diode. These charges diffuse in the device with time and also drift due to the electric field. This produces current in the device. Therefore, the reverse-biased diode conducts current following the ion strike. Current flowing through the diode after the strike is shown in Figure 19. Note that the Gaussian profile of the introduced charge shown in Figure 19 peaks at 2 ps with a standard deviation of 0.3 ps. The entire charge is deposited within first 5 ps.
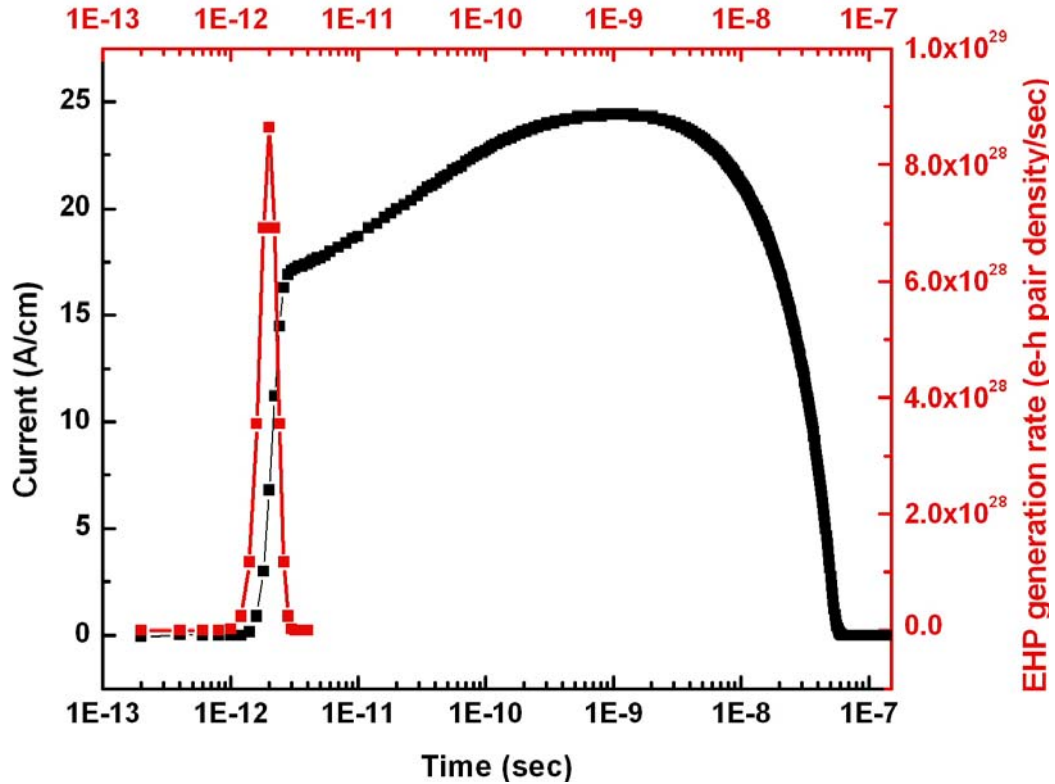
Figure 19 Density of strike-induced electron-hole pairs deposited in time indicating complete charge deposition within first 5 ps (in red). Transient current following this charge deposition is also plotted (-4000 V, LET= 0.71).

The energy deposited during the ion strike creates a large number of electron-hole pairs along the ion track. Generated carriers inside the track neutralize the fixed charges inside the depletion region that intersects with the ion track. The ion track acts as a conductor. A linear voltage drop occurs along the ion track. Also the electric field within the depletion region decreases.

The generation of a large number of carriers leads to an initial increase in current. The deposited carriers drift due to the electric field. The carriers diffuse in the radial direction due to the concentration gradient. The electrons move toward the n^+-contact & holes drift

toward the p$^+$-contact. Therefore, the current increases at short times as the carriers begin to separate and drift toward the contacts. However, at the end of the ion track, the carrier density decreases as the carriers move out of the device, allowing the field to increase locally. The increasing electric field eventually approaches the critical field for impact ionization. This initiates impact ionization near the high field area. The generation of carriers due to impact ionization results in increased charge, producing the secondary rise in current.

At long times, if most of the carriers in the track have diffused away or drifted out of the device without further addition of carriers, the current decreases. In most situations, the current eventually falls back to zero and the diode reaches its steady-state condition.

Role of impact ionization model in ion strike simulations

Impact ionization is a very important mechanism that generates additional electron-hole pairs in reverse-biased power diodes where high electric field gradients are present. Ion-strike simulations are performed with and without the impact ionization model to understand the contribution of avalanche-generated charge to the overall current in the device.

A current trace simulated with and without impact ionization keeping all the other parameters same is plotted in Figure 20. An increase in the current flowing through the diode is observed when the impact ionization model is included. The secondary rise in

current mentioned previously is evident from Figure 20. Increase in the current was

expected as avalanche-generated carriers contribute to the total current.
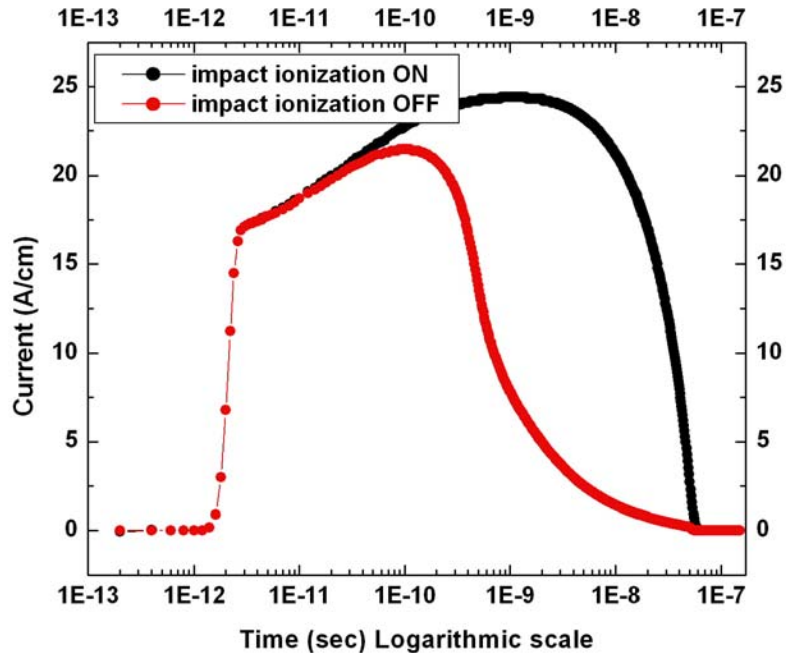

Figure 20 Contribution of avalanche-induced charge on current transients through diode
after strike

Total charge collected during the strike can be estimated by integrating the temporal

current profile. Difference in the integrals of two current transients gives the avalanche-

generated charge. Figure 21 shows the temporal profile of current due to the avalanche-
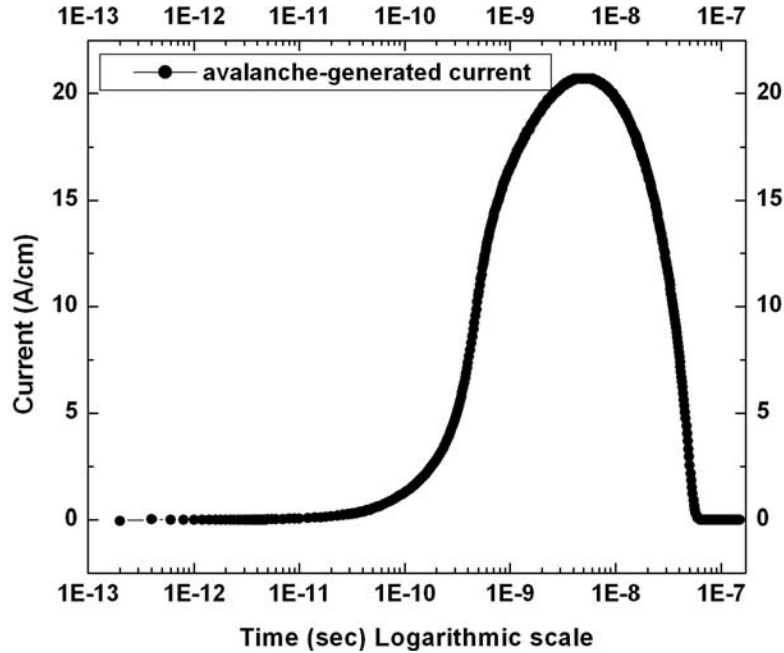
induced charge.

Figure 21 Current flowing through the diode only due to avalanche-induced charge.

Figure 22 demonstrates that the initial rise in the current following the passage of an ion depends on the applied bias. For the same number of ion-induced carriers, the initial increase in the current is greater for higher applied bias. As the applied bias on the diode increases, the electric field inside the diode increases. Thus more carriers are removed from the diode immediately after the strike under the influence of larger electric fields producing higher currents. The secondary rise in current due to impact ionization is also higher for larger applied biases. The increase in the impact ionization rate with applied bias [equation 19] explains the higher secondary current for larger bias. The increase in secondary current is small as temperature effects are included, which is explained later in this work.
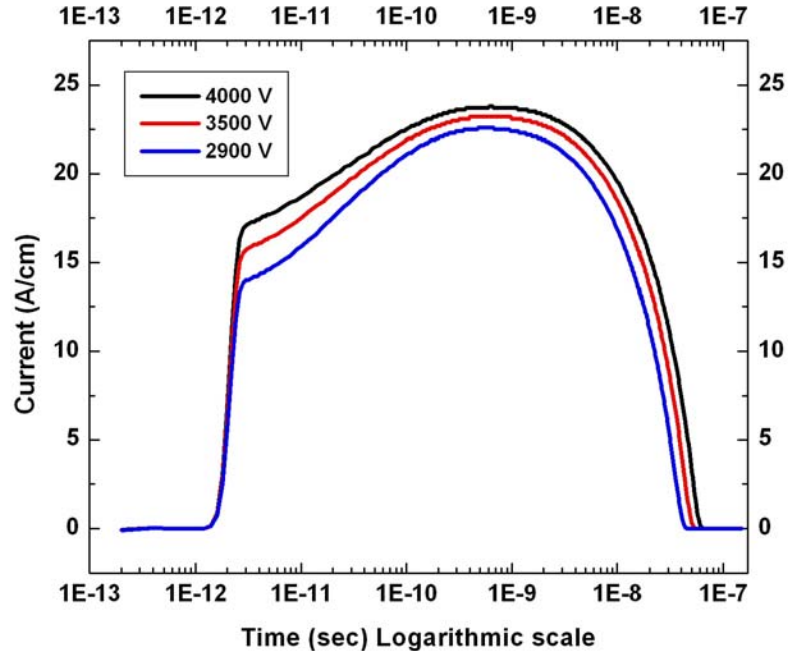
Figure 22 Current transients for applied biases of 2900 V, 3500 V and 4000 V

Effect of temperature on strike-induced current transients

Power diodes are subjected to temperature increase after an ion strike because large electric fields and higher carrier concentrations lead to self-heating. Isothermal ion strike simulations at three different temperatures were performed to observe the changes in device characteristics with temperature, keeping all other parameters the same. Current transients obtained at three different temperatures are plotted in Figure 23.

Figure 23 Effect of temperature on current transients simulated at 300 K, 400 K and 500 K.

It is observed that current through the diode decreases for higher temperatures, but for the same blocking voltage and LET values. Decrease in the current 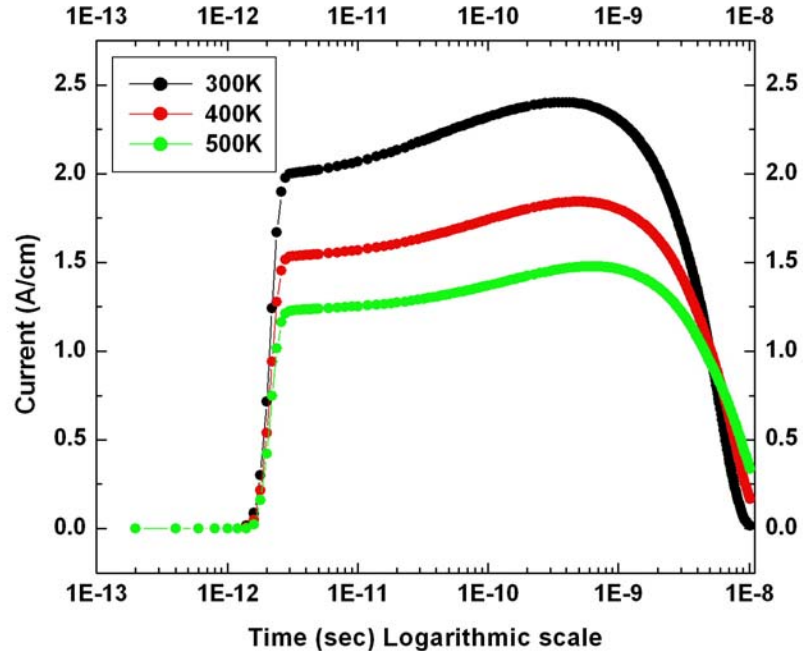is explained by the temperature dependence of the carrier mobility. Drift velocity decreases with increase in temperature because of increased lattice scattering, resulting in a decrease in current. Maximum current is observed at later times for higher temperatures. The time required to remove all excess charge is longer with high temperature because of the reduced drift velocity. Charge collected for different times at three different temperatures is listed in Table 1. Collected charge is estimated by integrating the current transients. It is observed that less charge is collected at higher temperatures for a given time compared to that at lower temperatures because of the slower transport of the charge. Note that the current dropped to almost zero for 300 K in 10 ns indicating no more charges are collected at the

contacts. However, for higher temperatures larger current shows that charges are still being collected at the contacts. This is due to reduced drift velocity at higher temperature.

Table 1 Charge collected in different time after ion strike

Temperature (K)	Charge collected in time (C/cm)			
	10 ps	100 ps	1 ns	10 ns
300	1.6×10^{-11}	2.17×10^{-10}	2.35×10^{-9}	1.09×10^{-8}
400	1.22×10^{-11}	1.63×10^{-10}	1.8×10^{-9}	1.04×10^{-8}
500	9.75×10^{-12}	1.28×10^{-10}	1.44×10^{-9}	9.53×10^{-9}

<u>Non-isothermal ion strike simulation</u>

Self-heating effects during an ion strike on a diode were simulated when device temperature was not restricted to a particular temperature. The effect of self heating on device characteristics was examined. Current transients for the diode biased at 4000 V with and without self-heating effects are shown in Figure 24. Peak temperature inside the diode is monitored in time. For the diode biased at 4000 V, the peak temperature occurred at 32 ns. The temperature distribution inside the diode at 32 ns is shown in Figure 25. The initial rise in current due to ion-induced charges is the same with inclusion and exclusion of self-heating effects. Avalanche-induced generation starts when the electric field increases locally. The localized heating is observed due to large electric field and current near the intersection of the ion track and the *pn* junction inside the base region. A local temperature rise is observed due to self-heating effects. As the local

temperature increases, a decrease in current is observed due to reduced carrier mobility. For the diode biased at 4000 V, avalanche-induced current peaks at 5 ns, while peak temperature is observed at 32 ns. Even after the avalanche-generated carrier concentration peaks, the electric field increases as carriers move. Increase in the electric field in the presence of carriers leads to further self-heating. Intrinsic carrier concentration also increases with temperature. Increase in the carrier concentration and decrease in the carrier mobility at higher temperatures are two competing processes. Maximum temperature is reached when local carrier concentration is reduced significantly to reduce self-heating and temperature starts to decrease. The temperature distribution inside the diode at 32 ns shows that the localized high temperature region extends only 1 μm along radial direction away from the strike. The thermal penetration depth for transient simulation times of the order of 1.5×10^{-7} sec is $l_{th} = \sqrt{\kappa t} \approx 3.6$ μm, where κ (0.87 cm^2/s) is the thermal diffusivity of silicon. Because the penetration depth is much smaller than the diode dimensions, the boundary condition does not affect the thermal response.
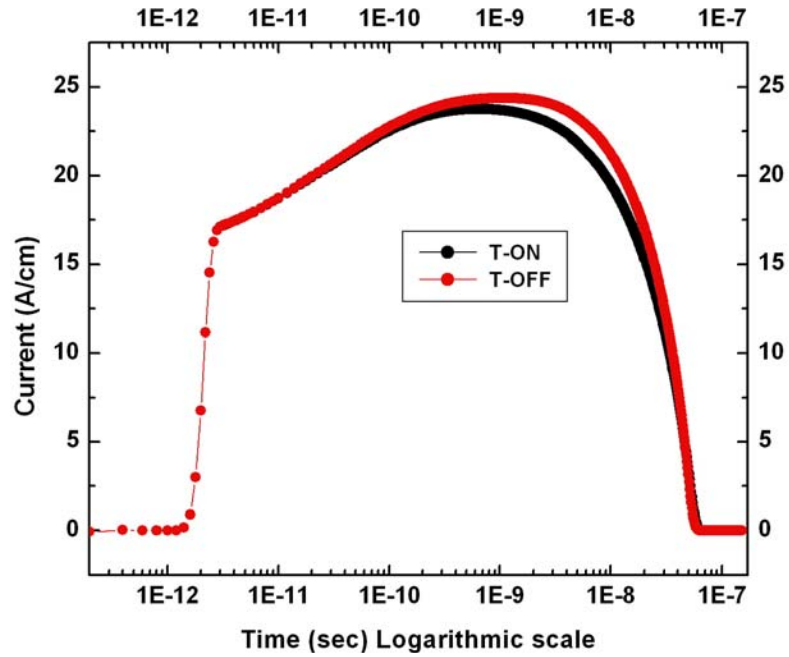
Figure 24 Comparison of current transients with and without self-heating effects at 4000 V applied bias.
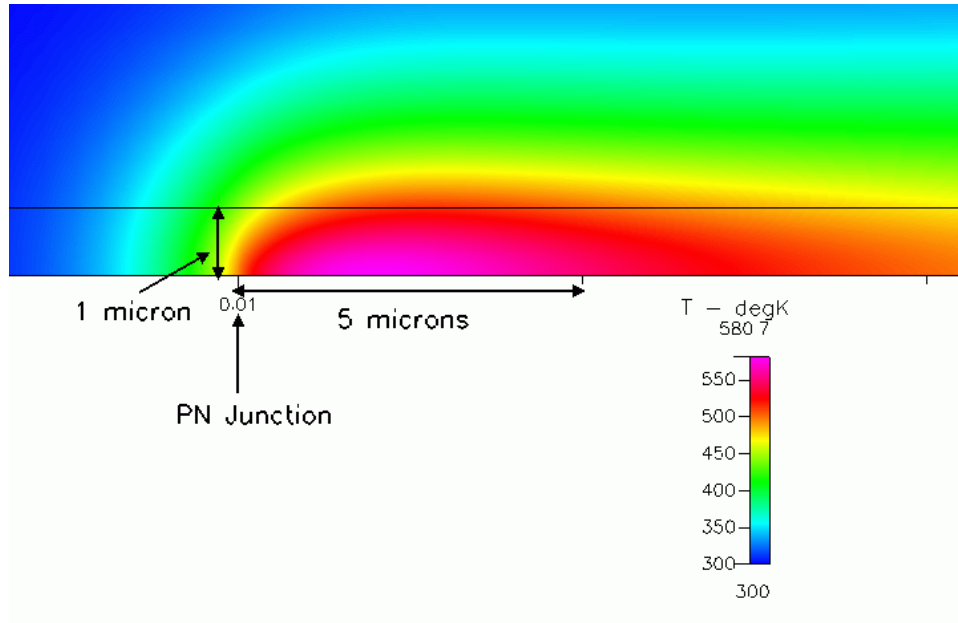

Figure 25 Temperature distribution near pn junction at 32 ns after strike at 4000 V.

Self-heating effects were studied as a function of applied bias. Applied bias values of 2900 V, 3500 V, and 4000 V were chosen because single-event burnout was observed experimentally when the diode was biased higher than 3000 V. Current transients observed for these three applied biases are compared in Figure 26. Electric field and electron density along plane of incident ion inside the hot spot are monitored in time and shown in Figure 27 and Figure 28. The temperature distribution inside the diode was monitored in time. Peak temperatures observed in the diode are plotted in Figure 29. Current through the diode was higher for larger applied bias, however it returned to zero for all three applied biases. Current and temperature inside the diode decrease after the initial rise suggesting thermal runaway did not occur. Avalanche-generated charge increases with bias. Thus the results are consistent as more charge was collected for higher applied biases. Evolution of electric field seen in Figure 27 indicates that maximum 300 kV/cm electric field was observed within 0.5 μm from interface. However, inside the hotspot (1-3 μm) maximum electric field was less than 200 kV/cm. Critical electric field for impact ionization is ~ 1000 kV/cm. Thus electric field inside the diode was not high enough to generate considerably large number of avalanche-generated carriers. Secondary current rise, primarily because of avalanche-generated charge, was not considerably different for lower applied biases. Self-heating is calculated from product of local current density and electric field. Although difference is not large, higher peak temperatures were observed due to the higher generation rate for larger biases. Intrinsic carrier concentration increases with temperature. For the temperatures generated in these simulations (~ 575 K), intrinsic carrier concentration is $\sim 3 \times 10^{15}$ cm^{-3}. This is much lower than the deposited carrier density. Therefore intrinsic carrier concentration

doesn't contribute directly to the overall current and temperature rise reported here. Eventual recovery of diode to the normal operating current (reverse leakage current) and temperature after ion strike suggested survival of diode.
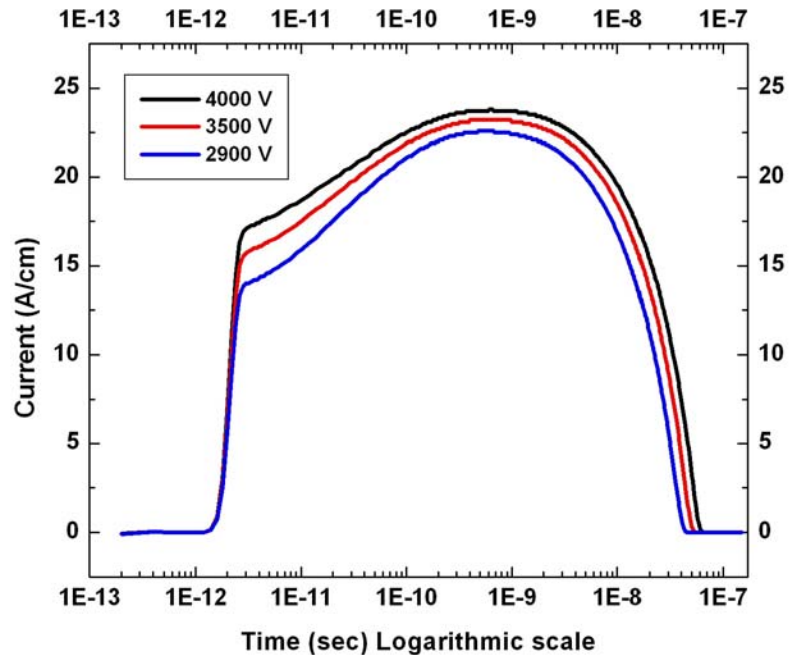

Figure 26 Current transients with inclusion of self-heating effects for 2900 V, 3500 V, and 4000 V
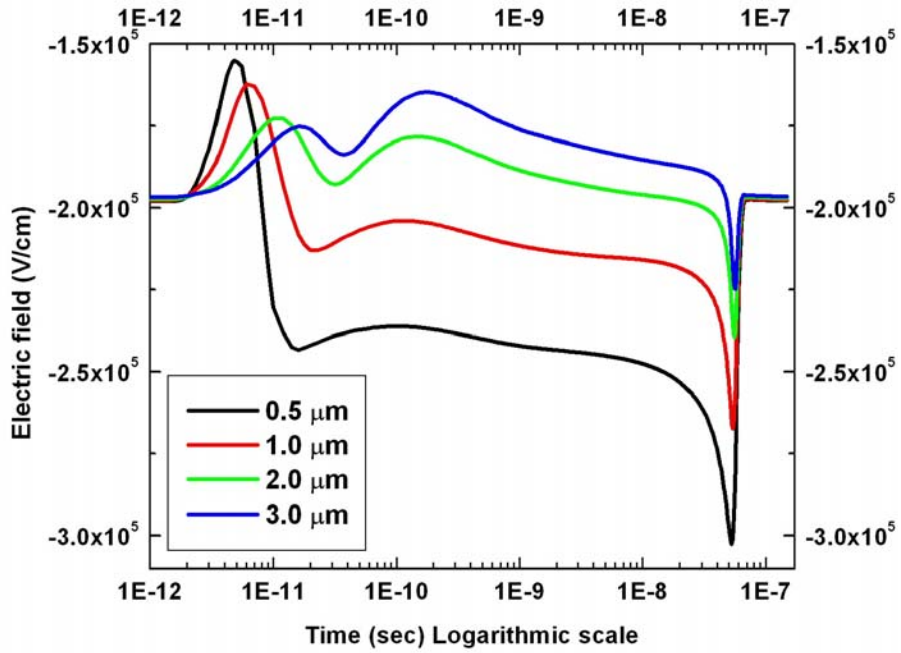
Figure 27 Electric field at a distance from p^+-n^- interface inside n^- region in the plane of incident ion (4000 V case)
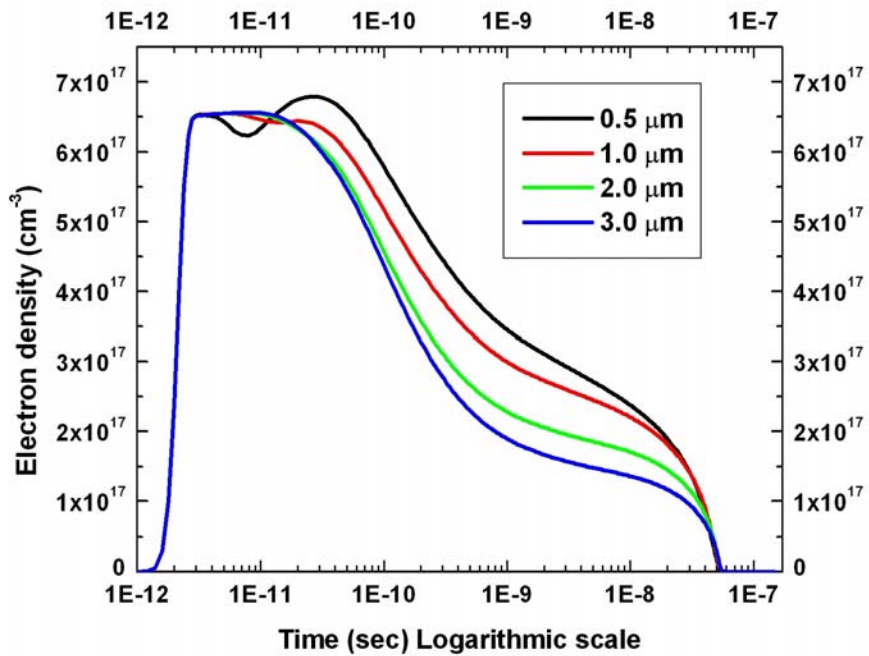

Figure 28 Electron density at a distance from p^+-n^- interface inside n^- region in the plane of incident ion (4000 V case)

A higher peak temperature for a larger bias suggests avalanche-induced charge is responsible for the temperature rise. The short term current rise immediately after the strike is insignificant because a large number of strike-induced carriers reduce the electric field. As the carriers near the junctions are being removed, electric field begins to increase. The temperature rises considerably as avalanche-induced carriers are created. Also, it is important to note that the temperature peak occurred later in time for higher applied biases. This indicates that the impact ionization mechanism is the driving force for self-heating, not the strike-induced charge.
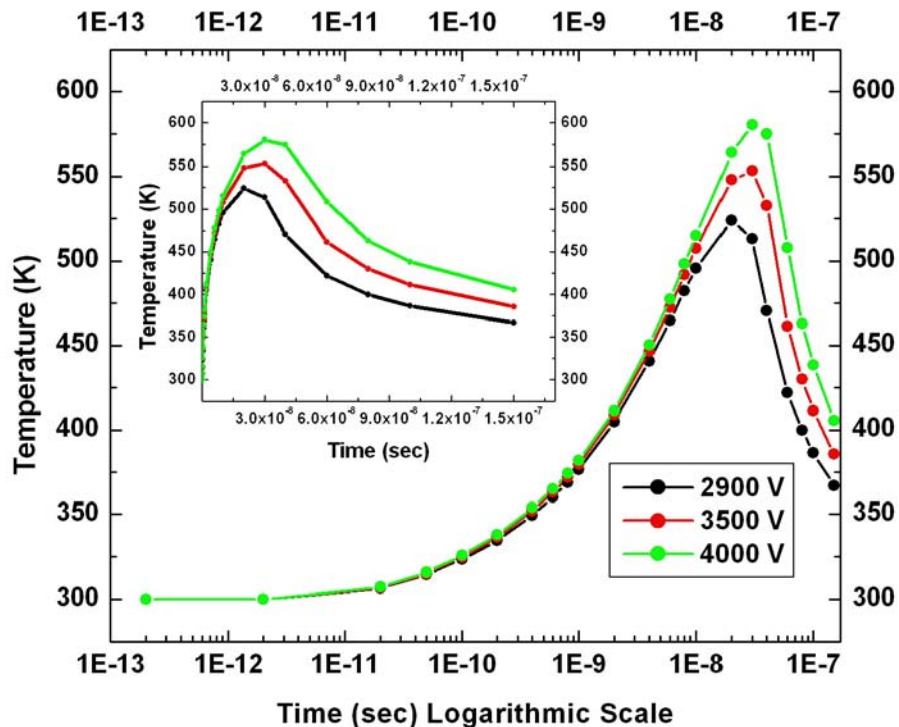

Figure 29 Peak temperatures inside the device at different time after the strike for applied biases of 2900 V, 3500 V and 4000 V. Same plot on linear time scale is shown in the inset.

Comparison of 2D and 3D simulation models

As described before, the charge density deposited along the track due to the strike is the same for 2D and 2D axi-symmetric simulation models. The current induced following the strike has drift and diffusion components. Drift component of current density is unaffected by dimensionality of 2D rectangular and axi-symmetric simulation models because electric field distribution is same in the two cases. However diffusion of charge is dependent on dimensionality of the model. Therefore charge diffusion gradients would vary for the two simulation models resulting in different diffusion current density. To obtain incite into the dimensionality issue, the transient diffusion equation was examined for charge diffusion in 2D and 2D axi-symmetric models using Green's functions. Constant electron diffusivity of 36.254 cm^2/s ia employed in calculations. The deposited charge is normalized to unity inside the ion track. Figure 30 and Figure 31 show charge profiles for 2D rectangular and axi-symmetric models away from the strike axes at different times. It is observed that immediately after charge deposition (up to 1×10^{-13} s) charge profiles look the same. Also the charge is confined within ~150 nm, which is the ion track radius. For later times it is observed that the charge inside the track region reduces sooner in 2D axi-symmetric model (Figure 31) than 2D rectangular model (Figure 30). Thus diffusion component of current density is expected to be higher in axi-symmetric case. Also the local electric field inside the track is reduced immediately after the strike because of a large amount of deposited charge. As the charge diffuse out, the electric field would reestablish faster in 2D axi-symmetric case. Thus increased localized current densities along with electric field may lead to more self-heating. Therefore 2D rectangular simulations may have under-predicted temperatures.
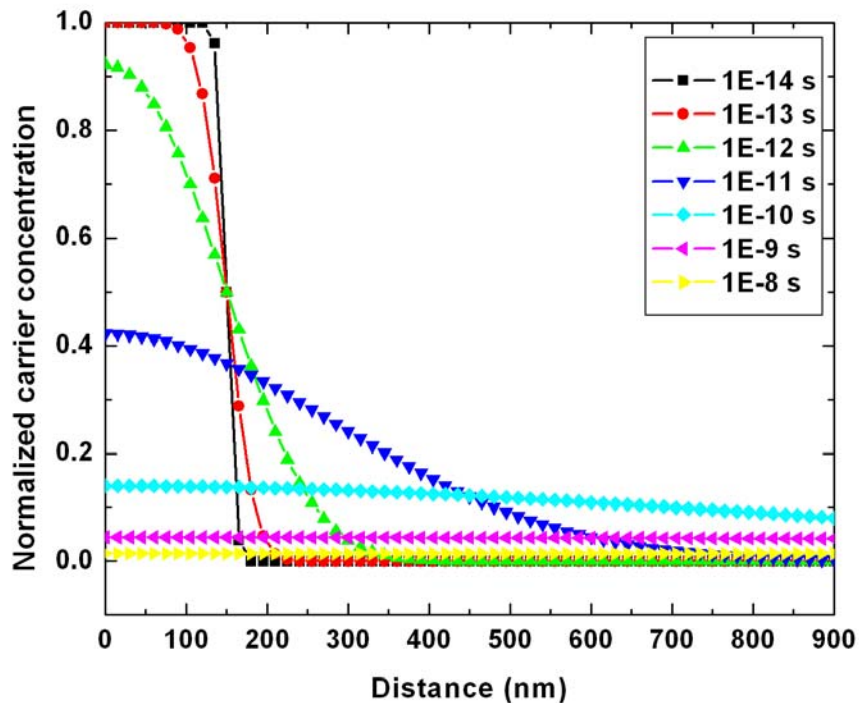
Figure 30 Normalized carrier concentration inside 2D rectangular diode away from the axis of ion strike at different times.
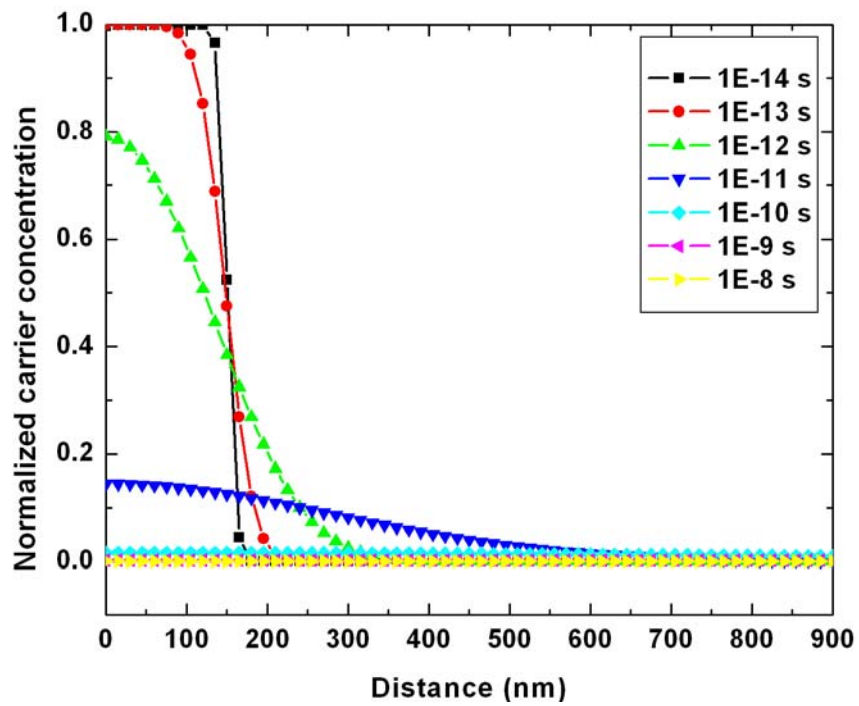

Figure 31 Normalized carrier concentration inside 2D axi-symmetric diode away from the axis of ion strike at different times.

CHAPTER V

CONCLUSION

The main objective of the present work was to study single-event burnout mechanisms in power diodes. A 2D rectangular diode structure, similar to a diode structure for which burnout failure was observed experimentally, was studied with device-based simulations. Transient ion-strike simulations were performed where the diode current was observed in time. Ion-strike parameters were chosen based on experimental data. Temperature dependence was included through coupled electro-thermal models to observe the effects of internal device temperature on device characteristics and to study burnout mechanism.

Self-heating effects inside the diode were simulated with coupled electro-thermal simulations. Parameters such as carrier mobility, intrinsic carrier concentration and impact ionization rate are dependent on temperature. Variation in temperature inside the diode affects the electrical characteristics of the diode. Simulations predicted lower current at larger temperatures assuming isothermal conditions. A decrease in the transient diode current for higher temperatures is attributed to reduced carrier mobility due to increased lattice scattering. For higher temperatures, current returned to zero later in time compared to low temperatures because of reduced carier drift velocity. The induced charge is removed slower for higher temperatures due to reduced carrier drift velocity. Intrinsic carrier concentration increases for higher temperature because more electrons have sufficient energy to overcome the bandgap. Impact ionization rate is lower for high

temperatures. However, this effect is not included in the above simulations. Thus these are competing effects when thermal dependence is included.

Avalanche-induced charge has a significant contribution on the transient current through diode. The observed secondary rise in current is due to the avalanche-generated charge. Large currents in the presence of large electric fields lead to localized heat generation. This resulted in a localized increase in diode temperature. Peak temperatures inside the diode occurred after the peak of avalanche-induced charge was observed. An increase in temperature is attributed to the avalanche-induced charge that leads to self-heating of the diode. Avalanche-generated charge is greater for larger applied biases because of high electric fields. For larger applied biases, peak temperatures inside the diode are higher. This is a result of higher heat generation rates for larger biases. Again, avalanche-induced charge is responsible for self-heating.

Intrinsic carrier concentration, which is a function of temperature, increases in a localized region. Increase in carrier concentration does not contribute to current increase in the diode and does not lead to further heating because the electric field is reduced. Thus the diode doesn't enter into a thermal feedback loop as originally hypothesized [18].

The present device-level simulations including self-heating effects did not identify thermal feedback as the failure mechanism for power diodes. Working within the capabilities of simulations tools, based on the assumptions made and parameters chosen, it was observed that self-heating effects play negligible role in powder diode burnout.

However, more accurate simulations need to be performed before complete exclusion of self-heating effects for burnout studies. The current simulations emphasize the importance of impact ionization modeling because impact ionization induced charge is responsible for heating of the diode. Localized heating also affects the total charge generated.

There are several parameters that can be improved in further studies. The 2D simulations described here were conducted using rectangular coordinates, which simulate the ion strike as an infinite sheet of charge, unlike in the true 3D situation. Simple comparison of charge diffusion in 2D rectangular and 2D axi-symmetric models suggests that 2D rectangular simulations could have under-predicted temperatures inside the diode after strike. Thus the temperature profile would be different due to altered heat generation rate and profile. This will influence electrical characteristics of the diode. Thus further 2D axi-symmetric and possibly full 3D simulations are necessary. The ion track structure generated based on the ion energy deposited along its path is required. Temperature-dependent impact ionization model needs to be included for future studies.

REFERENCES

1. Stassinopoulos EG and Raymond JP. The Space Radiation Environment for Electronics. Proceeding of the IEEE 1988; 76(11):1423-42.

2. Fleetwood DM and Winokur PS. Radiation Effects in the Space Telecommunications Environment. Proceedings of the 22nd International Conference on Microelectronics 2000; 1: 43-9.

3. Zeller HR. Cosmic ray induced failures in high power semiconductor devices. Solid-State Electronics 1995; 38(12):2041-6.

4. Ziegler J, Lanford W. The effect of sea level cosmic rays on electronic devices. IEEE International Digest of Technical Papers 1980; 23:70-1.

5. Waskiewicz AE, Groninger JW, Strahan VH, Long DM. Burnout of power mos transistors with heavy ions of 252-Cf. IEEE Transactions on Nuclear Science 1986; 33:1710-3.

6. Roubaud F, Dachs C, Palau JM, Gasiot J, Tastet P. Experimental and 2D simulation study of of the single-event burnout in n-channel power MOSFET's. IEEE Transactions on Nuclear Science 1993; 40(6):1952-8.

7. Dachs C, Roubaud F, Palau JM, Bruguier G, Gasiot J. Evidence of the ion's impact position effect on seb in n-channel power mosfets. IEEE Transactions on Nuclear Science 1994; 41(6):2167-71.

8. Johnson GH, Schrimpf RD, Galloway KF. Temperature dependence of single-event burnout in n-channel power MOSFETs. IEEE Transactions on Nuclear Science 1992; 39(6):1605-12.

9. Johnson GH, Hohl JH, Schrimpf RD, Galloway KF. Simulating single-event burnout of n-channel power MOSFET's. IEEE Transactions on Electron Devices 1993; 40(5):1001-8.

10. Kabza H, Schulze HJ, Gestenmaier Y, Voss P, Wilhelmi J, Schmid W et al. Cosmic radiation as a possible cause for power device failure and possible countermeasures. Proceedings of 6th International Symposium on power Semiconductor Devices & IC's 1994; 9-12.

11. Zeller HR. Cosmic ray induced failures in high power semiconductor devices. Microelectronics Reliability 1997; 37(10):1711-18.

12. Brand H and Selberherr. Two-Dimensional Simulation of Thermal Runaway in a Nonplanar GTO-Thyritor. IEEE Transactions on Electron Devices 1995; 42(12):2137-46.

13. Voss P, Maier KH, Becker HW, Normand E, Wert JL, Oberg DI et al. Irradiation experiments with high voltage power devices as a possible means to predict failure rates due to cosmic rays. Proceedings of the IEEE International Symposium on power Semiconductor Devices & IC's 1997; 169-73.

14. Busatto G, Iannuzzo F, Wyss J, Pantano D and Bisello D. Effects of Heavy Ion Impact on Power Diodes. Radiation and Its Effects on Components and Systems 1999; 205-9.

15. Soelkner G, Voss P, Kaindl W, Wachukta G, Maier KH and Becker HW. Charge Carrier Avalanche Multiplication in High-Voltage Diodes Triggered by Ionizing Radiation. IEEE Transactions on Nuclear Science 2000; 47(6):2365-72.

16. Kuboyama S, Matsuda S, Kano T, Ishii T. Mechanism for single-event burnout of power MOSFETs and its characterization technique. IEEE Transactions on Nuclear Science 1992; 39(6):1698-1703.

17. Albadri AM, Schrimpf RD, Walker DG, and Mahajan SV. Coupled electro-thermal simulations of single event burnout in power diodes. IEEE Transactions on Nuclear Science 2005; 52(6): 2194-2199.

18. Albadri AM, Walker DG, Fisher TS, and Schrimpf RD. Simulation of single event failure in power diodes. Proc. Int. Mechanical Engineering Congress Expositions, New Orleans, LA 2002; 17-22.

19. Muller RS and Kamins TI. Device electronics for Integrated Circuits. 3rd ed. John Wiley and Sons; 2003.

20. CFD Research Corporation. CFD-ACE+ User Manual V2003. Huntsville, Alabama 35805, 2003.

21. Caughey DM and Thomas RE. Carrier mobilities in silicon empirically related to doping and field. Proceedings of IEEE 1967; 55: 2192-2193

22. Dziewior J and Schmid W. Auger coefficients for highly doped and highly excited silicon. Applied Physics Letters 1977; 31:346-348.

23. McKay KG, McAfee. Electron multiplication in Silicon and Germanium. Physical Review 1953; 91(5):1079-84.

24. Sze SM. Physics of Semiconductor Devices. 2nd ed. John Wiley and Sons; 1981.

25. Biersack JP, Ziegler JF. SRIM Version 2003.26: Pergamon Press, 2003.

26. http://tvdg10.phy.bnl.gov/LETCalc.html

27. Fageeha O, Howard J, Block RC. Distribution of radial energy deposition around the track of energetic charged particles in silicon. Journal of Applied Physics 1994; 75(5):2317-21.

28. Canali C, Majni G, Minder R, and Ottaviani G. Electron and hole drift velocity measurements in silicon and their empirical relation to electric field and temperature. IEEE Transactions on electron Devices 1975; 11:1045-47.